



UNIVERSIDADE ESTADUAL DE CAMPINAS
Faculdade de Engenharia Elétrica e de Computação

Tcharllys Viana de Sousa

Spatial Modeling of Non-Diffracting Beams in GHz and THz: Theory, Generation, and Possible Medical Application.

Modelamento espacial de feixes não-difrativos em GHz e THz: teoria, geração e possível aplicação médica

Campinas

2020



UNIVERSIDADE ESTADUAL DE CAMPINAS
Faculdade de Engenharia Elétrica e de Computação

Tcharllys Viana de Sousa

Spatial Modeling of Non-Diffracting Beams in GHz and THz: Theory, Generation, and Possible Medical Application.

Modelamento espacial de feixes não-difrativos em GHz e THz :teoria, geração e possível aplicação médica

Dissertation presented to the School of Electrical and Computer Engineering of the University of Campinas in partial fulfillment of the requirements for the degree of Master in Electrical Engineering, in the area of Telecommunication and Telematics.

Dissertação apresentada à Faculdade de Engenharia Elétrica e de Computação da Universidade Estadual de Campinas como parte dos requisitos exigidos para a obtenção do título de Mestre em Engenharia Elétrica, na Área de Telecomunicações e Telemática.

Supervisor: Prof. Dr. Michel Zamboni Rached

Este exemplar corresponde à versão final da tese defendida pelo aluno Tcharllys Viana de Sousa, e orientada pelo Prof. Dr. Michel Zamboni Rached

Campinas

2020

Ficha catalográfica
Universidade Estadual de Campinas
Biblioteca da Área de Engenharia e Arquitetura
Luciana Pietrosanto Milla - CRB 8/8129

So85s Sousa, Tcharllys Viana de, 1995-
Spatial modeling of non-diffracting beams in GHz and THz : theory, generation, and possible medical application / Tcharllys Viana de Sousa. – Campinas, SP : [s.n.], 2020.

Orientador: Michel Zamboni Rached.
Dissertação (mestrado) – Universidade Estadual de Campinas, Faculdade de Engenharia Elétrica e de Computação.

1. Análise de ondas localizadas. 2. Propagação de ondas. 3. Física ótica. 4. Eletromagnetismo na medicina. I. Zamboni Rached, Michel. II. Universidade Estadual de Campinas. Faculdade de Engenharia Elétrica e de Computação. III. Título.

Informações para Biblioteca Digital

Título em outro idioma: Modelamento espacial de feixes não-difrativos em GHz e THz : teoria, geração e possível aplicação médica

Palavras-chave em inglês:

Localized waves analysis

Wave propagation

Physical optics

Electromagnetism in medicine

Área de concentração: Telecomunicações e Telemática

Titulação: Mestre em Engenharia Elétrica

Banca examinadora:

Michel Zamboni Rached [Orientador]

Erasmus Recami

Cesar Jose Bonjuani Pagan

Data de defesa: 30-04-2020

Programa de Pós-Graduação: Engenharia Elétrica

Identificação e informações acadêmicas do(a) aluno(a)

- ORCID do autor: <https://orcid.org/0000-0002-5677-8343>

- Currículo Lattes do autor: <http://lattes.cnpq.br/4503734629481635>

COMISSÃO JULGADORA - DISSERTAÇÃO DE MESTRADO

Candidato: Tcharllys Viana de Sousa RA: 209406

Data da Defesa: 30 de Abril de 2020

Título da Tese: Spatial Modeling of Non-Diffracting Beams in GHz and THz: Theory, Generation, and Possible Medical Application.

Título da Tese: Modelamento Espacial de Feixes Não-Difrativos em GHz e THz: Teoria, Geração e Possível Aplicação Médica.

Prof. Dr. Michel Zamboni Rached (Presidente)

Prof. Dr. Erasmo Recami

Prof. Dr. Cesar Jose Bonjuani Pagan

A ata de defesa, com as respectivas assinaturas dos membros da Comissão Julgadora, encontra-se no SIGA (Sistema de Fluxo de Dissertação/Tese) e na Secretaria de Pós-Graduação da Faculdade de Engenharia Elétrica e de Computação.

I dedicate this work to the working class of my country, specially those who did not have the opportunity to attend college.

Acknowledgements

Since I arrived in Campinas I have been facing an emotional roller-coaster of good and terrible experiences that ultimately led to this work. And, I must not forget the people that helped me get through this ride. Specially because this dissertation was only possible because of the help, love and generosity of them. Therefore, I would like to use this space to thank them.

Firstly, I am grateful to my mother, Alzenir Viana de Sousa, for all the support and encouragement that I have received so far in life. She was the one who most battled against capitalism, homophobia, and machism with me. She taught me to speak, read, write, and to believe.

I am grateful to my boyfriend Bruno Malveira Peixoto. He was “the one I treated the worst only because he loved me the most”. Thank you for all the love and care at any moments and specially during my frequent emotional breakdown.

I thank my friends, Amanda Monteiro, Amanda Thayla, Janaina Ferreira, Jaynne Pessoa, João Luis, Jonatas Macêdo, Laís Sousa, Surama Costa, Yasmin Leite that have been with me at all times and slowly became family to me.

I thank my advisor Michel Zamboni Rached for the opportunity of joining his team, for excellent classes and for believing on this research.

I thank professor Erasmo Recami and professor Hugo Enrique Hernández Figueroa for all the knowledge they shared with me in our brief meetings.

I thank my laboratory partners for all the joy-full chats, support, help and tips.

I thank the best president of Brazil’s history Luís Inácio Lula da Silva and president Dilma Vana Rousseff for facilitating my ingress on a public university and for Science without Borders exchange program, respectively.

I thank CNPq under the grant 169796/2017-5, and Unicamp for the financial support.

This study was financed in part by the grant 2017/20644-0, São Paulo Research Foundation (FAPESP).

This study was financed in part by the Coordenação de Aperfeiçoamento de Pessoal de Nível Superior – Brasil (CAPES).

Lastly, I thank my favorite singers Taylor Swift, Lorde, Lana del Rey, Florence Welch,

and Lady Gaga for composing and singing the songs that help me to stay sane.

*“ You say that dreamers always get what they desire
Well I’ve found, the more I want the less I’ve got
(FOSTER, Mark)*

Abstract

Despite the increasing efforts in studying non-diffracting optical beams, much less work has been done in the characterization and application of these beams for millimeter and sub-millimeter wavelengths. This is because, in order to generate these beams for long distances, large equipment and antennas are required. However, if shorter distances are considered (Fresnel region), interesting and useful diffraction-resistant beams can be generated with smaller antennas. In this work, by using scalar and vectorial approaches, we obtain analytical solutions describing plane waves, Gauss, Bessel-Gauss, and Bessel beams truncated by circular apertures, for GHz and THz frequencies. Moreover, this work aims at characterizing, simulating, and commenting possible applications of such truncated beams. These applications are aimed into to possible medical applications, such as hyperthermic treatments. Lastly, this paper presents a redesign of an antenna capable of generating truncated Bessel Beams.

Keywords: Localized waves analysis; Wave propagation; Physical optics; Electromagnetism in medicine.

Resumo

Apesar dos esforços crescentes no estudo de feixes ópticos resistentes à difração, poucos trabalhos foram realizados na caracterização e aplicação desses feixes para comprimentos de onda milimétricos e submilimétricos. Isso ocorre porque, para gerar tais feixes por longas distâncias, são necessários grandes equipamentos e antenas. No entanto, se forem consideradas distâncias mais curtas (região de Fresnel), feixes resistentes à difração podem ser gerados com antenas menores. Neste trabalho, usando abordagens escalares e vetoriais, obtemos soluções analíticas descrevendo ondas planas, feixes de Gauss, Bessel-Gauss e Bessel truncados por aberturas circulares, para frequências de GHz e THz. Além disso, este trabalho tem como objetivo caracterizar, simular e comentar possíveis aplicações de tais feixes truncados. Essas aplicações são direcionadas para possíveis aplicações médicas, como tratamentos hipertérmicos. Por fim, esta dissertação apresenta um redesenho de uma antena capaz de gerar feixes de Bessel truncados.

Keywords: Análise de ondas localizadas; Propagação de ondas; Física ótica; Eletromagnetismo na medicina.

List of Figures

Figure 1 – Depth of field for initial spot beams of 60 m and wavelength 0.66 m for: (a) Gaussian beam (b) feasible Bessel beam.	17
Figure 2 – Comparison between the desired intensity pattern in the longitudinal direction and the pattern obtained with the Frozen Wave.	18
Figure 3 – 3D graph of the field strength in the longitudinal direction for the obtained Frozen Wave.	19
Figure 4 – Representation of Durnin’s Experiment for the generation of Bessel Beams.	20
Figure 5 – a) Emanating field for a 50 GHz circularly truncated plane wave. b) Initial field for a 50 GHz truncated plane wave with $R = 10$ cm.	44
Figure 6 – a) Emanating field for a 100 GHz circularly truncated Gauss beam. b) Initial field for a 100 GHz truncated Gauss beam with $R = 5$ cm.	45
Figure 7 – a) Emanating field for a 200 GHz truncated Bessel-Gauss beam. b) Initial field for a 200 GHz truncated Bessel-Gauss beam with $R = 10$ cm.	45
Figure 8 – a) Emanating field for a 300 GHz circularly truncated Bessel beam. b) Initial field for a 300 GHz truncated Bessel beam with $R = 15$ cm.	46
Figure 9 – Top view of a dielectric filled PPW with slit grating. Each slit has a width w_s and its center is positioned in relation to the center of the antenna from a distance ρ_s	48
Figure 10 – Cross-sectional view of the proposed structure. The green arrows represent the fields that are leaking away from the antenna as the outward waves propagates.	53
Figure 11 – Cross-sectional view of the proposed dielectric filled PPW. The light blue diamond shape represents the spatial region in which the Bessel Beam is formed as a result of interference of the leaked field.	53
Figure 12 – Top and cross-sectional view of the considered structure along with its physical and geometrical parameters.	54
Figure 13 – 1D periodic metallic strip grating.	55
Figure 14 – Normalized attenuation constants obtained via dispersion analysis for different strip widths.	56
Figure 15 – Normalized phase and attenuation constants for the proposed parameters: $w = 5mm$, $d = 16mm$, $h = 3.14mm$, and $\epsilon_r = 2.2$	57
Figure 16 – Detailed view of the feeding structure simulated on CST Microwave Studio.	58

Figure 17 – For $f = 10GHz$: a) Normalized 3D visualization of the radiating field $ E_z $. b) Color map of the absolute value of E_z	59
Figure 18 – Simulated 3D visualization of $ E_z $ at the transverse plane $z = 100mm$	60
Figure 19 – Simulated 2D profile of $ E_z $ at the transverse plane $z = 100mm$	60
Figure 20 – 1D beam profile at the line $y = 0mm$ and $z = 100mm$ of an ideal Bessel beam (dotted black line) and the radiated beam (red line).	61
Figure 21 – a) Orthogonal projection of the transverse electric field radiated by the antenna according to simulation on <i>CST Microwave Studio</i> at the frequency of 10GHz. b) Simulated 2D profile for the transverse electric field at the transverse plane $z = 100mm$	62
Figure 22 – 1D beam profile at the line $y = 0$ and $z = 100$ of an ideal first order Bessel beam (dotted black line) and the radiated transverse electric field (red line).	62
Figure 23 – a) Orthogonal projection of the absolute value of the electric field $ E $ radiated by the antenna according to simulation on <i>CST Microwave Studio</i> . b) 3D profile of $ E $ at the plane $z = 100mm$	63
Figure 24 – a), c) and e): Orthogonal projection of $ E_z $ radiated by the antenna according to simulation on <i>CST Microwave Studio</i> for $w = 4mm$, $w = 6mm$, and $w = 7mm$, respectively. b), d) and f): Normalized 3D profile of the radiated $ E_z $ for $w = 4mm$, $w = 6mm$, and $w = 7mm$, respectively.	64
Figure 25 – Calculated spectra $S(k_z)$ for a continuous Frozen Wave at the frequency of 50GHz.	69
Figure 26 – a) 3D view and b) Orthogonal projection of the continuous Frozen Wave profile propagating on an absorptive medium at the frequency of 50GHz.	69
Figure 27 – Calculated spectra $S(k_z)$ for a compensated continuous Frozen Wave at the frequency of 50GHz.	70
Figure 28 – a) 3D view and b) Orthogonal projection of the compensated continuous Frozen Wave profile propagating on an absorptive medium at the frequency of 50GHz.	71
Figure 29 – a), c), and e) Orthogonal projection of the compensated continuous Frozen Wave propagating on absorptive medium with complex index $n_i = 0.005$, $n_i = 0.01$, $n_i = 0.02$, respectively. The non-compensated case is presented on b), d), and f).	72
Figure 30 – Depth of penetration of a plane wave into the human skin for the range of frequency of 1GHz to 20GHz along with the wavelength λ according to the data retrieved from (GABRIEL <i>et al.</i> , 1996).	74

Figure 31 – Index of reflection of the human skin for the range of frequency of 1GHz to 20GHz along with the wavelength λ according to the data retrieved from (GABRIEL <i>et al.</i> , 1996).	75
Figure 32 – Depth of penetration of a plane wave into the human skin for the range of frequency of 0.1THz to 1.5THz along with the wavelength λ according to the data retrieved from (LIN, 2011).	76
Figure 33 – Index of reflection of the human skin for the range of frequency of 0.1THz to 1.5THz along with the wavelength λ according to the data retrieved from (LIN, 2011).	76

List of Tables

Table 1 – Initial field excitation for important particular cases of localized waves . .	40
Table 2 – Depth of propagation for a plane wave propagating through absorptive media with different complex refractive indices.	71

Contents

1	Introduction	16
1.1	Context	16
1.2	Motivation	20
1.3	Objectives	22
1.3.1	General Objectives	22
1.3.2	Specific Objectives	22
1.4	Reading Guides	23
2	Literature Review	24
2.1	Introduction to Electromagnetic Beams	24
2.1.1	Gaussian Beam	24
2.1.2	Bessel Beam	26
2.1.3	Frozen Waves	28
2.1.3.1	Discrete Frozen Waves	29
2.1.3.2	Continuous Frozen Waves	30
2.2	Effect of Millimeter and Sub-Millimeter Waves in Human Body	33
2.2.1	The Terahertz Region	33
2.2.2	Terahertz-Tissue Interaction	33
2.2.2.1	Interaction at a Cellular Level	34
2.2.3	Thermal Energy Induced in Tissues by Electromagnetic Waves	34
2.2.3.1	Thermal Damage to Cells and Tissues	36
3	Generation of Beams Truncated by Finite Apertures in Millimeter and Sub-millimeter Wavelengths	38
3.1	Scalar Approach	39
3.2	Ensuring the Validity of the Scalar Approach	42
3.3	Results and Discussions	43
3.3.1	Analytic Description of the Truncated Plane Wave	43
3.3.2	Analytic Description of the Truncated Gauss Beam	44
3.3.3	Analytic Description of the Truncated Bessel-Gauss Beam	44
3.3.4	Analytic Description of the Truncated Bessel Beam	44
4	Generation of Bessel Beams: A Redesign of an Antenna Model	47
4.1	Introduction	47
4.2	Design Foundation and Field Evaluation	48
4.3	Antenna Proposal	52

4.3.1	Design Criteria	55
4.3.2	Feed Design	57
4.4	Simulated Results	58
4.5	Further Investigations	62
5	Millimeter and Sub-millimeter Continuous Frozen Waves in Absorbing Medium	66
5.1	Results	68
6	Analysis of the Interactions Between Non-Diffracting Waves and Biological Tissue	73
	Conclusion	78
6.1	Future Perspectives	79
	Bibliography	80

1 Introduction

1.1 Context

Diffraction and attenuation of electromagnetic beams are well known and studied phenomena and their effects often limit the use of these waves. Respectively, diffraction and attenuation cause a progressive increase of the transverse width and the reduction of the intensity. (BORN; WOLF, 2013)

In order to mitigate such physical effects, studies are carried out proposing different types of spatial modeling of the electromagnetic beams. In this context, the so-called localized waves or non-diffracting waves, which are solutions of the wave equation (and also of Maxwell's equations), were first obtained in theory and then they were produced in laboratories. (HERNÁNDEZ-FIGUEROA *et al.*, 2007)

Non-diffracting waves (beams and pulses) are those that have the ability to maintain the same transverse pattern over a long distance (HERNÁNDEZ-FIGUEROA *et al.*, 2007). In free space or in material media (RECAMI; ZAMBONI-RACHED, 2009), so, they can be considered resistant to the diffraction effects observable in the usual beams. This is due to the space-time structure that these waves possess; the lateral portions of the beam (or pulse), when they diffract, are able to reconstruct their central region. (LÓPEZ-MARISCAL; GUTIÉRREZ-VEGA, 2007)

It should be noted that, for the most part, the theory and experiments related to non-diffracting waves have been and continue to be concentrated at optical frequencies. As we shall see shortly, it is part of our proposal to carry out a transposition / adaptation of theory and experimental generation to the GHz and THz regimes.

The best-known example of a diffraction resistant wave is the Bessel beam. In practice, such beams, indefinitely resistant to diffraction, are not feasible since an infinite amount of energy would be required for their generation (ZAMBONI-RACHED, 2006). However, it has been theoretically and experimentally proven, see for example (SALEM *et al.*, 2011; DURNIN *et al.*, 1987; BUTKUS *et al.*, 2002), the possibility of generating truncated Bessel Beams; that is, generated by a finite aperture. Thus, optimal approximations are obtained for the ideal Bessel Beams propagating resisting the effect of diffraction over long distances (LÓPEZ-MARISCAL; GUTIÉRREZ-VEGA, 2007; STRATTON, 1941). Thus, beams of this type may be interesting substitutes for Gaussian beams in different types of applications (SALEM

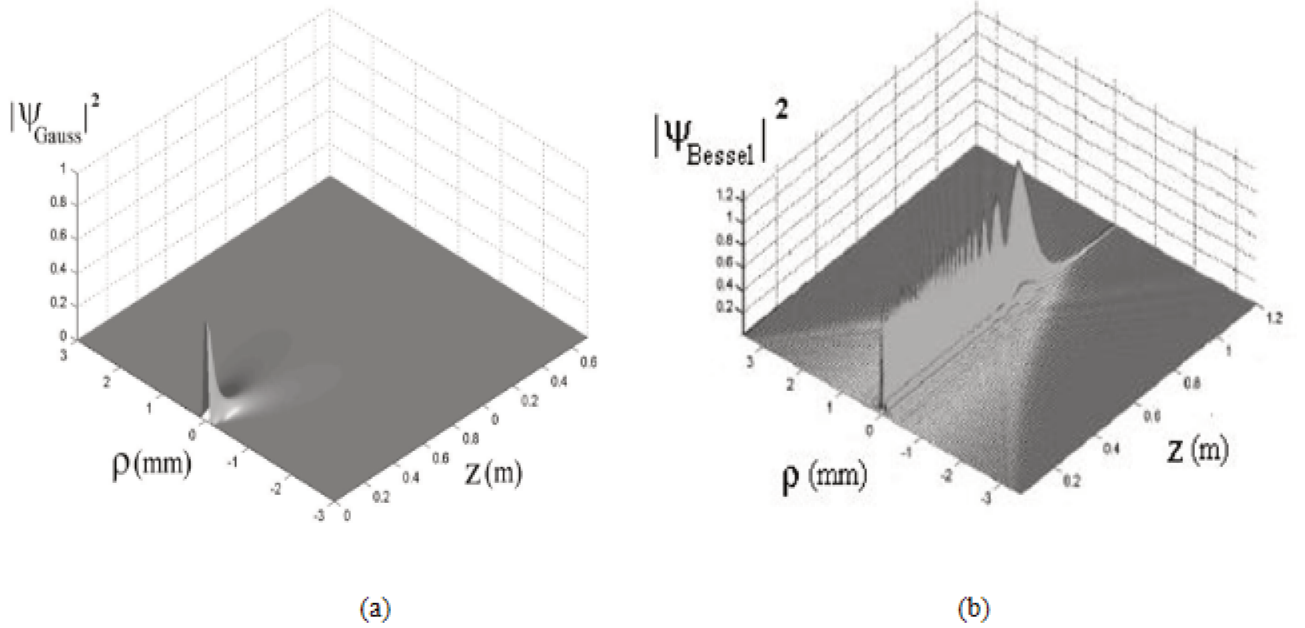


Figure 1 – Depth of field for initial spot beams of 60 μm and wavelength 0.66 μm for: (a) Gaussian beam (b) feasible Bessel beam.

et al., 2011).

It is shown on Figure 1 the comparison between a Gaussian beam and a Bessel beam, both truncated by a 3.5mm aperture. It is possible to verify that, in the case of beams with the same initial spot (60 μm) and the same wavelength (0.66 μm), the depth of the Gaussian beam is only 3cm, while that of the Bessel beam is 85cm.

In general, the non-diffracting characteristic of Bessel Beams is desirable in several application as, for instance: optical manipulation, remote sensing, confined beam spectroscopy, high resolution hyperthermia for surfaces or internal tissues, generation of non-ionizing images, etc. (FUSCALDO *et al.*, 2016; DATTA *et al.*, 2015)

Besides its resistance to transverse broadening, a Bessel Beam suffers attenuation when propagating in an absorbing media. Nonetheless, sometimes it is desirable that some regions of the propagation axis be more radiated than others and, even more desirable, if this feature is achieved by using only one source, resulting in a spatially structured beam resistant to diffractive effects and also to the attenuation effect caused by the medium.

It was in this sense that a very interesting technique, named *Frozen Waves*, was theoretically developed and experimentally confirmed in the optical regimes (ZAMBONI-RACHED, 2004; ZAMBONI-RACHED *et al.*, 2005; ZAMBONI-RACHED, 2006; VIEIRA *et*

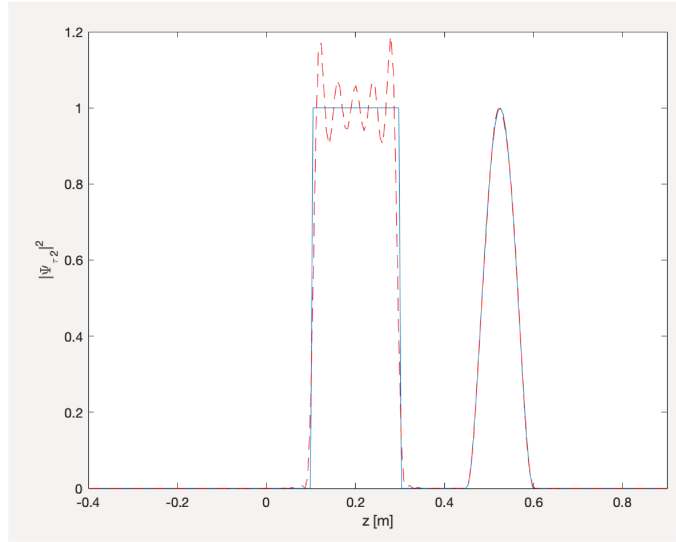


Figure 2 – Comparison between the desired intensity pattern in the longitudinal direction and the pattern obtained with the Frozen Wave.

al., 2012; DORRAH *et al.*, 2016a). Using this method it is possible to obtain optical beams (in absorbing media) resistant to diffraction and attenuation whose longitudinal intensity pattern can be chosen at will.

In summary, Frozen Waves beams are obtained from the superposition of co-propagating Bessel beams of the same frequency but with different complex amplitudes and different transverse and longitudinal wave numbers (DORRAH *et al.*, 2016a). It is shown in Zamboni-Rached (2004), Zamboni-Rached *et al.* (2005) that, once one does this superposition, it is possible to construct an envelope of static intensity which takes on almost any desired shape within a given spatial range $0 \leq L \leq z$, where z is the propagation axis and L a distance, in general, much greater than the wavelength λ . As an example, it is shown in Figure 2, in continuous line, an example of desired longitudinal pattern; while the pattern obtained from the modeling of 28 superimposed Bessel Beams is shown in dotted line. In this example, the desired pattern in the longitudinal was a step and a parable. It is evident that the resulting beam, besides being resistant to the diffraction effects (because its spot does not undergo enlargement), has a longitudinal pattern of intensity approximately equal to the desired one. It is shown in Figure 2.24 the 3D pattern of the Frozen Wave.

The possibility of modeling, on demand, the beam longitudinal intensity pattern, even though it is in an absorbent medium, makes the Frozen Waves also considered to be resistant to attenuation. Although energy absorption by the propagation medium still occurs, these beams have the capacity to reconstruct their nucleus by considerably greater distances than other types of optical beams (diffractive or non-diffractive) (ZAMBONI-RACHED *et*

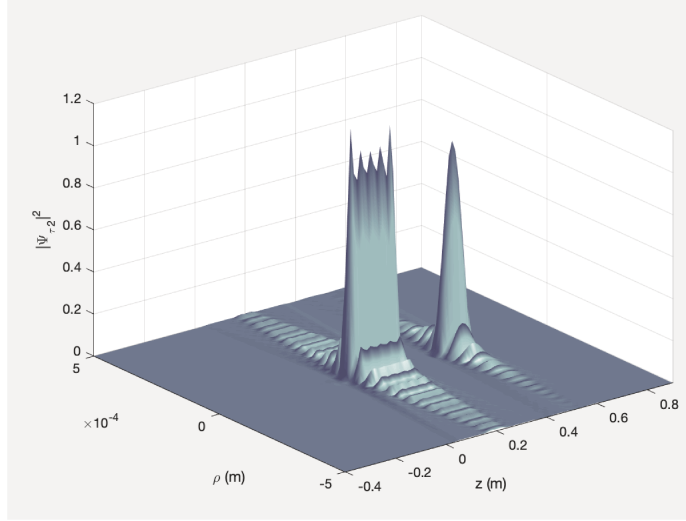


Figure 3 – 3D graph of the field strength in the longitudinal direction for the obtained Frozen Wave.

al., 2005; ZAMBONI-RACHED, 2006). As can be seen in Figure 2, the wave intensity is obtained in the desired patterns. Thus, it is possible to implement beams that deliver power, that is, have the desired field strength, only in certain regions of the longitudinal axis. The experimental verification of these beams was obtained in (VIEIRA *et al.*, 2012; DORRAH *et al.*, 2016a), thus opening numerous applications possibilities, namely: remote sensing (MUGNAI *et al.*, 2000), optical tweezers (AMBROSIO; HERNÁNDEZ-FIGUEROA, 2011; AMBROSIO; ZAMBONI-RACHED, 2015), optical guidance of atoms (PACHON *et al.*, 2016), optical communications (GARAY-AVENDAÑO; ZAMBONI-RACHED, 2016), etc.

Of course, the implementation of these special beams in microwave and millimeter wave regimes would open new possibilities for applications of great interest, such as in remote sensing (in such frequencies), orbital angular momentum control and its use for communications and also medical applications.

In the literature, there exists a few studies for the generation of Bessel beams in the microwave range, as shown in (RANFAGNI *et al.*, 2004; HERNÁNDEZ-FIGUEROA *et al.*, 2007; SALEM *et al.*, 2011). However, the generation of Frozen Waves in this frequency range has not been formulated theoretically and experimentally in spite of its benefits; since that at low frequencies, in comparison to the optical frequencies, antennas need to be relatively large, thus limiting their application (LEMAÎTRE-AUGER *et al.*, 2011); in addition, despite the promising future for the millimeter waveband, as the next generation of high-speed short distance communication systems, very few studies of ways to generate Bessel beams in this frequency range have been made so far.

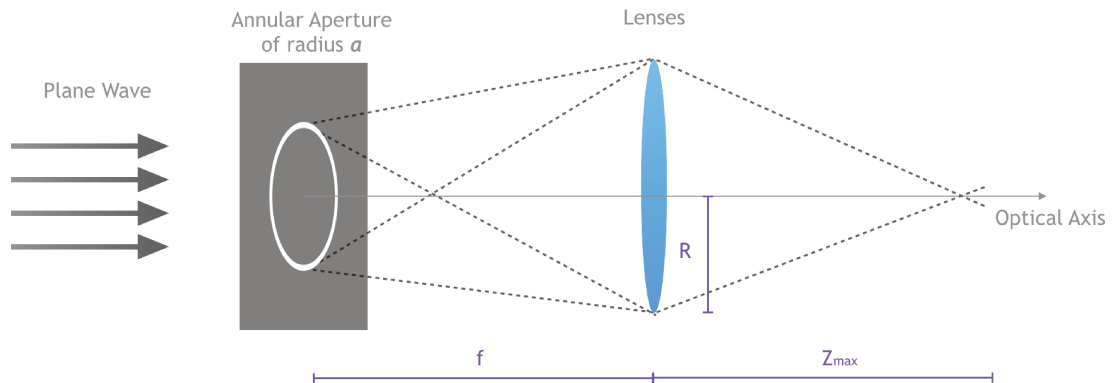


Figure 4 – Representation of Durnin's Experiment for the generation of Bessel Beams.

In order to fill up these gaps, this project aims to find scalar and vectorial solutions to Bessel beams in GHz and THz frequencies for the truncated case. Then, we will use these results to design an aperture antenna capable of generating such beams. Besides, it aims to find scalar and vectorial solutions to Frozen Waves in GHz and THz wavelengths. Lastly, we will study the field irradiation at biological tissues, verify its effects and propose medical applications for beams in the aforementioned wavelength ranges.

1.2 Motivation

The main purpose of this master's thesis is the study and development, specially through theory and simulations, of techniques for the spacial modelling of electromagnetic beams in the millimeter and sub-millimeter waves. It also aims to analyse an antenna capable of generating the theoretically obtained beams, as well as possible applications. In order to do so, it will be presented solutions to the Maxwell Equations that give support for the initial hypothesis of the generation of Bessel Beams and also the so-called *Frozen Waves* in the GHz and THz frequency range.

Over the time, several techniques for the generations of non-diffracting beams have been developed. The first of then was Durnin's experiments, that consisted in interposing to a plane wave a annular aperture positioned in the focal plane of a convergent lens, as it is shown in Figure 4 below. However, in this method of generations, there are high power losses due to the fact that most part of the energy is blocked by the diffracting ring (DURNIN *et al.*, 1987)

Given the inherent limitations of Durnin's method of generating Bessel Beams, over the time new methods have been developed. An example is the use of conical lens (axicons) to generate Bessel Beams. Other method is the holography, which replaces the axicons, as can be seen in (VASARA *et al.*, 1989; HERNÁNDEZ-FIGUEROA *et al.*, 2007; ISHIMARU, 2017).

Despite the rising interest in the study of non-diffracting optical beams and pulses, little has been done in the millimeter and sub-millimeter. In part, this is justified because, in order for such beams to be generated in these frequency bands over long distances and using known methods, it would be required the use of relatively large equipment making the technique not very attractive.

However, there may be interesting applications in the GHz and THz frequency bands in which the required propagation distances are small, such as in medical applications. In such cases, the process of generating beams resistant to the diffraction and attenuation phenomena (and spatially modeled) could, at first, be made with smaller and more technically and economically feasible antennas.

Therefore, it is fundamental to find, for Maxwell's Equations, solutions of diffraction resistant beams that can be spatially modeled, even if they propagate in absorbent media (thus, making it possible to obtain beams whose spots are also resistant to attenuation by long distances). This is because, from these mathematical solutions to the electromagnetic beams, it will be possible to idealize and simulate prototypes of antennas capable of generating such waves.

Of course, the study of the generation of non-diffractive beams in the frequencies mentioned above leads to questions about possible applications to them. At this point, this work aims to study, in a preliminary way, the possibility of using such beams as activators of the hyperthermic effect in internal tissues. When analysing waves in the range of THz, for example, they are found to have electromagnetic properties necessary for the health sciences; since their energy levels are very low (1-12 meV), and, therefore, cellular damages are reduced to thermal effects. (SIEGEL, 2004)

The benefits of hyperthermic treatment in the fight against cancer are explicated in (STEGER; BOO-CHAI, 1990; ALEKSEEV *et al.*, 2008; SOARES *et al.*, 2014). However, one of the main obstacles to the clinical use of hyperthermic therapy is the difficulty in obtaining more defined heating points with greater spatial and temporal control; as a consequence, many researchers in the field of oncology consider hyperthermia a very complicated form of treatment to be used (RHOON *et al.*, 2016). Therefore, it is necessary to develop technologies that meet the current clinical demands and enable the use of this form of treatment.

Due to its long distance attenuation resistance and the greater possibility of power control being delivered in different regions along the propagation axis, Frozen Waves type beams are important substitutes for existing technologies and have the prospect of satisfying the technical demands for the use of hyperthermia, especially in more internal tissues. (DORRAH *et al.*, 2016a; DORRAH *et al.*, 2016b) Thus, that these beams need to be studied and designed for the GHz and THz frequencies.

1.3 Objectives

1.3.1 General Objectives

- To study analytically the electromagnetic beams in the frequencies of THz and GHz in order to obtain exact solutions to Maxwell's equations;
- To contribute with the study of non-diffracting beams, especially in the range of GHz and THz;
- To study Frozen Waves in GHz and THz aiming to model it in regions with the wavelength size order;
- To study the possibility of generation of Bessel beams in GHz;
- To attest the generation of the hyperthermic effect from beams in millimeter and sub-millimeter wave.

1.3.2 Specific Objectives

- To make a bibliographical review about non-diffraction beams and their main forms of generation;
- To develop hypotheses and formulate exact solutions for the wave equation for Bessel and Frozen Waves beams in the millimeter sub-millimeter frequency bands;
- To simulate, in CST Microwave Studio and / or MATLAB, the non-diffraction beams theoretically proposed, together with a proposed antenna that has the function of generating them;
- To continue the development of optical beam research at the State University of Campinas.

1.4 Reading Guides

This work is divided in 6 chapters. Following this brief introduction, chapter 2 summarizes the topics and knowledge that are required for the complete understanding of this work. In Chapter 3, a theoretical description of Truncated Bessel Beams in GHz and THz frequency is provided. In Chapter 4, we suggest an mean of generation of the beams discussed on the previous chapter via the design of an 10 GHz Leaky Wave antenna. In Chapter 5, we suggest a theoretical description of Continuous Frozen Waves when propagating trough absorptive medium. In chapter 6 we analyze the possibility of generation of Frozen Waves on biological Tissues. For closure, there is a conclusion and future perspectives section.

2 Literature Review

2.1 Introduction to Electromagnetic Beams

In this section we are going to present the fundamental concepts involving the electromagnetic beams that are going to be cited/used in this dissertation.

This section is divided into three subsections. The first covers an important ordinary beam, the Gaussian Beam (NEWELL, 2018). The second covers one of the most renowned non-diffraction wave: the Bessel beam (HERNÁNDEZ-FIGUEROA *et al.*, 2007). Lastly, we introduce a technique to model the shape of stationary wave fields; or, in other words, the Frozen Wave (ZAMBONI-RACHED, 2004).

2.1.1 Gaussian Beam

In this subsection we present the Gaussian Beam by constructing its solution using super-positions of plane waves. In the scalar case, the Gauss Beam is made of plane waves that propagate in directions that goes from 0° to 90° with respect to the direction of propagation (which is the "+z" direction).

Initially, we consider an Electric Field given by:

$$\vec{E}(\vec{r}, t) = E_{y0} e^{i\vec{k}\cdot\vec{r}} e^{-i\omega t} \hat{y} \quad (2.1)$$

where:

$$k^2 = k_x^2 + k_y^2 + k_z^2 = \frac{\omega^2}{c^2} \quad (2.2)$$

It is clear that Equation 2.1, jointly with Equation 2.2, obeys the wave equation; however, it does not obey Gauss's Law. Hence, the Electric Field can not be given by Equation 2.1 and needs to be corrected.

In order to do so, we need to suppose an Electric Field component in the \hat{z} direction, whose value is easily obtained by using Gauss Law. It results in Equation 2.3 below:

$$E_z = - \int \frac{\partial E_y}{\partial y} dz \quad (2.3)$$

Next, we will do a superposition of these waves in which they have the same frequency and propagate in directions parallel to $\vec{k} = k_x\hat{x} + k_y\hat{y} + k_z\hat{z}$. We are going to work with the component of the Electric field in the \hat{y} direction (Equation 2.1) while the component E_z can be calculated using Equation 2.3.

We need to consider now a \vec{E} given by $\vec{E} = E_y\hat{y} + E_z\hat{z}$, in which E_y is described on Equation 2.4 bellow.

$$\vec{E}_y = e^{-i\omega t} \int_{-\frac{\omega}{c}}^{\frac{\omega}{c}} dk_y \int_{-\sqrt{\frac{\omega}{c}-k_y^2}}^{\sqrt{\frac{\omega}{c}-k_y^2}} dk_x \Lambda(k_x, k_y) e^{ik_x x} e^{ik_y y} e^{iz\sqrt{\frac{\omega}{c}-(k_x^2+k_y^2)}} \hat{y} \quad (2.4)$$

Note that, in Equation 3.18, $k_z = \sqrt{\frac{\omega}{c} - (k_x^2 + k_y^2)}$ in order to select only the positive contributions. Also, the limits of the integrals were selected in order to guarantee that k_x , k_y and k_z are real.

In summary, the solution to Equation 3.18 clearly depends on the spectrum $\Lambda(k_x, k_y)$. Then we are going to define the spectrum as:

$$\Lambda(k_x, k_y) = \frac{r_0^2}{4\pi} e^{-\frac{r_0^2}{4}k_x^2} e^{-\frac{r_0^2}{4}k_y^2} \quad (2.5)$$

It is clear that the spectrum that we chose is a product of two Gaussian functions centered in $k_x = k_y = 0$.

Unfortunately, it is not possible to find an exact solution to Equation 3.18 when the spectrum is given by Equation 2.5; however, we can make the following approximations:

1. The spectrum will only have appreciable values when k_x and k_y are much smaller than $\omega/c = k$, hence:

$$\sqrt{\frac{\omega^2}{c^2} - (k_x^2 + k_y^2)} \approx \frac{\omega}{c} - \frac{(k_x^2 + k_y^2)^2}{2\omega/c} \quad (2.6)$$

2. Write the integration limits as:

$$\int_{-\infty}^{\infty} dk_y \int_{-\infty}^{\infty} dk_x \quad (2.7)$$

With these paraxial approximations one can solve Equation 3.18 as:

$$E_y = \frac{e^{ik(z-ct)}}{\left(1 + \frac{2iz}{kr_0^2}\right)} \exp\left[\frac{-\rho^2}{r_0^2\left(1 + \frac{2iz}{kr_0^2}\right)}\right] \quad (2.8)$$

Which is a mathematical description of a Gaussian Beam, pending the calculation of E_z (that can be performed using Equation 2.3).

Besides, we can verify that this beam suffers from transverse diffraction; and, it can be proved that it doubles the initial width (spot radius, $\Delta\rho_0$) after having traveled a certain distance z , called the diffraction length, expressed in Equation 2.9 below. (HERNÁNDEZ-FIGUEROA *et al.*, 2007)

$$z = \frac{\sqrt{3}k_0\Delta\rho_0^2}{2} \quad (2.9)$$

Finally, by looking at Equation 2.9 one can conclude that as more concentrated (smaller value for $\Delta\rho_0^2$) a Gaussian Beam is, the fastest it spreads itself.

2.1.2 Bessel Beam

In this section we are aiming to present and mathematically describe a Bessel Beam, which is a very well known example of non-diffracting beam. In order to do so, we start by considering the wave equation in rectangular coordinates, as follows in Equation 2.10. (BALANIS, 2012)

$$\frac{\partial^2\Psi}{\partial x^2} + \frac{\partial^2\Psi}{\partial y^2} + \frac{\partial^2\Psi}{\partial z^2} - \frac{1}{c^2} \frac{\partial^2\Psi}{\partial t^2} = 0 \quad (2.10)$$

What we are trying to accomplish here, is to use a correct superposition of plane waves to obtain a Bessel Beam. Initially, we consider a general and monochromatic solution to Equation 2.10 as demonstrated in Equation 2.11.

$$\Psi(x, y, z, t) = e^{-i\omega t} \int_{-\infty}^{\infty} dk_x \int_{-\infty}^{\infty} dk_y \int_{-\infty}^{\infty} dk_z e^{i\vec{k}\cdot\vec{r}} S(k_x, k_y, k_z) \quad (2.11)$$

where:

$$S(k_x, k_y, k_z) = \bar{S}(k_x, k_y, k_z) \delta\left[\sqrt{k_x^2 + k_y^2 + k_z^2} - \frac{\omega}{c}\right] \quad (2.12)$$

and $\bar{S}(k_x, k_y, k_z)$ is an arbitrary function of k_x , k_y , and k_z , i.e., the spectrum.

To deal with the mathematical difficulty we are going to perform the superposition noting that:

$$\vec{k} = k\hat{\mathbf{r}} = k[\cos\theta'\hat{\mathbf{z}} + \sin\theta'\cos\phi'\hat{\mathbf{x}} + \sin\theta'\sin\phi'\hat{\mathbf{y}}] \quad (2.13)$$

where $k = \omega/c$.

Then, we are going to make the following superposition:

$$\Psi(x, y, z, t) = e^{-i\omega t} \int_0^{2\pi} \int_0^\pi A(\theta', \phi') e^{i\vec{k} \cdot \vec{r}} d\theta' d\phi' \quad (2.14)$$

where $A(\theta', \phi')$ is the angular spectrum, and here it is chosen to represent wave vectors over a conical surface with aperture θ_0 :

$$A(\theta', \phi') = e^{in\phi'} \delta(\theta' - \theta_0) \quad (2.15)$$

That said, we can write

$$\Psi(x, y, z, t) = e^{-i\omega t} e^{ik \cos \theta_0 z} \int_0^{2\pi} e^{in\phi'} e^{ik \sin \theta_0 [x \cos \phi' + y \sin \phi']} d\phi' \quad (2.16)$$

Now, we transform the variables of Equation 2.16 from cylindrical to rectangular coordinates using the relations present on Equation 2.17:

$$\begin{cases} x = \rho \cos \phi \\ y = \rho \sin \phi \\ z = z \end{cases} \quad (2.17)$$

then, we obtain:

$$\Psi(\rho, \phi, z, t) = e^{-i\omega t} e^{ik \cos \theta_0 z} \int_0^{2\pi} e^{in\phi'} e^{ik \sin \theta_0 [\rho \cos \phi \cos \phi' + \rho \sin \phi \sin \phi']} d\phi' \quad (2.18)$$

Performing the change of variables given by $u = \phi' - \phi$, and using the trigonometrical identity of the cosine of the subtraction of two angles, we shall have:

$$\Psi(\rho, \phi, z, t) = e^{-i\omega t} e^{ik \cos \theta_0 z} e^{in\phi} \int_0^{2\pi} e^{inu} e^{i[k \sin(\theta_0)\rho] \cos u} du \quad (2.19)$$

Finally, we are now able to solve the integral on Equation 2.19, and find the expression for the Bessel Beam of the n^{th} order; presented on Equation 2.20.

$$\Psi(\rho, \phi, z, t) = A e^{-i\omega t} e^{ik_z z} e^{in\phi} J_n(k_\rho \rho) \quad (2.20)$$

where $k_\rho = k \sin(\theta_0)$, $k_z = k \cos(\theta_0)$; so, $k^2 = k_\rho^2 + k_z^2$.

As it was stated before, the Bessel Beam is a non-diffracting wave; which means that its transverse shape is invariant, i.e., resistant to diffraction while propagating, with spot (in the case of the zero-order) approximately given as:

$$\Delta\rho \approx \frac{2.405}{k_\rho} \quad (2.21)$$

Unfortunately, this specific solution to the wave equation can not be generated because it carries infinite energy flux. However, in this work, we will analyse Bessel Beams truncated by an aperture with radius R which are solutions that can be physically realized due to the finite amount of energy associated with the beam. It should be noted that, due to the limited energy associated to the beam, the non-diffraction property is limited to a certain range defined as

$$Z = \frac{R}{\tan \theta} \quad (2.22)$$

since $R \gg \frac{1}{k_\rho}$.

2.1.3 Frozen Waves

In this subsection we are going to present two types of localized waves, named Frozen Waves, that allow us to model the shape of wave fields. Both of them are found using superposition of equal-frequency Bessel Beams. The main difference between them is how these superposition are made; which changes its outcome. (ZAMBONI-RACHED, 2006)

The main goal here is to have $|\Psi(\rho = 0)|^2 = |F(z)|^2$ for any value of z where $F(z)$ is an arbitrary function.

The first example of this technique, so-called discrete Frozen Waves, is obtained by using a discrete superposition of Bessel Beams and aim to control the beam longitudinal intensity shape within a chosen interval $0 \leq z \leq L$; where, z is the propagation axis and L is a distance much greater than the wavelength. The fact that one is able to control the intensity until distances much farther than the wavelength guarantees that this solution to the wave equation has the capacity of propagating much farther than a Gaussian Beam or any other ordinary beam. (ZAMBONI-RACHED, 2004; ZAMBONI-RACHED *et al.*, 2005)

The second one, so-called discrete Frozen Wave, is obtained by using a continuous superposition of Bessel Beams and aim to control the beam longitudinal intensity shape within a very small portion of the propagation axis. This solution emerged from the necessity

of finding results for constructing a wave pattern over regions equivalent in size to a few times the wavelength that leads to highly non-paraxial beams. (ZAMBONI-RACHED *et al.*, 2017)

2.1.3.1 Discrete Frozen Waves

In order to describe mathematically a Discrete Frozen Wave, we start by taking into account the Bessel Beam from Equation 2.19.

By considering the superposition of $2N + 1$ beams at the same frequency, but with different k_z and k_ρ , we have:

$$\Psi(\rho, z, t) = Ae^{-i\omega t} \sum_{n=-N}^N J_0(k_{\rho n}\rho)e^{ik_{zn}z} \quad (2.23)$$

where $k_{\rho n}^2 = k^2 - k_{zn}^2$.

In these conditions, any longitudinal pattern express by a function $F(z)$ can be obtained by doing:

$$F(z) \approx \sum_{n=-N}^N A_n e^{i\frac{2\pi}{L}nz} \quad (2.24)$$

where $0 \leq z \leq L$.

Intuitively, it is desirable to make, in Equation 2.23, $k_{zn} = \frac{2\pi n}{L}$ because that would result in a simple Fourier Series when $\rho = 0$. However, that is not a good choice due to two reasons:

1. Once $n < 0$, the values for k_{zn} will be negative; hence, there will be undesired propagation in $-z$ direction.
2. This choice would not be appropriated for cases where $L \gg \lambda$.

Therefore, we choose:

$$k_{zn} = Q + \frac{2\pi n}{L} \quad (2.25)$$

where, Q is a value chosen accordingly to the situation ant the desired spot radius through Equation 2.26

$$Q = \sqrt{\left(\frac{\omega}{c}\right)^2 - \left(\frac{2.4}{\Delta\rho}\right)^2} \quad (2.26)$$

Thus, in order to satisfy the forward propagation requirements, we must have:

$$0 \leq Q + \frac{2\pi n}{L} \leq \frac{\omega}{c} \quad (2.27)$$

From Equation 2.27, we can identify the maximum number of terms for our series once we have chosen values for Q , L and ω .

Thereby, Equation 2.23 for $\rho = 0$ becomes:

$$\Psi(\rho, z, t) = e^{-i\omega t} e^{iQz} \sum_{n=-N}^N A_n e^{\frac{i2\pi n z}{L}} \quad (2.28)$$

Analysing Equation 2.28, it is clear that we have two exponential functions multiplied by a Fourier Series of $F(z)$. Hence, that results approximately in the desired beam; and the resulting field (Frozen Wave) is given by:

$$\Psi(\rho, z, t) = e^{-i\omega t} e^{iQz} \sum_{n=-N}^N A_n J_0(k_{\rho n} \rho) e^{\frac{i2\pi n z}{L}} \quad (2.29)$$

Lastly, it is not hard to show that, if we do the superposition indicated on Equation 2.29 but replacing the zeroth order Bessel beam for one with a higher order μ , we shall observe that the longitudinal intensity pattern shall be shifted to approximately $\rho = \rho_\mu$ from the axis $\rho = 0$, i.e.,

$$\Psi(\rho, z, t) = e^{-i\omega t} e^{iQz} \sum_{n=-N}^N A_n J_\mu(k_{\rho n} \rho) e^{i\mu\phi} e^{\frac{i2\pi n z}{L}} \quad (2.30)$$

and

$$|\Psi(\rho = \rho_\mu, z, t)|^2 \approx |F(z)|^2 \quad (2.31)$$

where

$$\rho_\mu = \frac{X_\mu}{\sqrt{k^2 - Q^2}} \quad (2.32)$$

with X_μ such that, $J_\mu(x)$ has its maximum value in $x = X_\mu$.

2.1.3.2 Continuous Frozen Waves

The so-called Continuous Frozen Wave is obtained by using a continuous superposition of Bessel Beams and aims to control the beam longitudinal intensity shape within a very

small portion of the propagation axis, i.e., over regions equivalent in size to a few times the wavelength, which leads to highly non-paraxial beams. (ZAMBONI-RACHED *et al.*, 2017; ZAMBONI-RACHED; RECAMI, 2008)

When we are taking into account highly non-paraxial beams configurations in which they are heavily focused, in general, it is not possible to treat them with paraxial theories, nor with scalar approaches (GARAY-AVENDAÑO; ZAMBONI-RACHED, 2014).

At this point, our goal is to present a mathematically simple approach capable of describing non-paraxial electromagnetic beams with fast convergence. For simplicity sake, we are taking into account only the scalar version of the method.

We start by considering a superposition of zero-order Bessel Beams, multiplied by a spectrum function $S(k_z)$, over the longitudinal wavenumber k_z .

$$\Psi(z, t) = e^{-i\omega t} \int_{-\omega/c}^{\omega/c} S(k_z) J_0\left(\rho \sqrt{\omega^2/c^2 - k_z^2}\right) e^{ik_z z} dk_z \quad (2.33)$$

What we are trying to do here is to obtain a $S(k_z)$, in Equation 2.33 and in its solution, that yield the following approximated longitudinal intensity pattern (except for a multiplicative constant):

$$|\Psi(\rho = 0, z, t)| \approx |F(z)|^2 \quad (2.34)$$

In Equation 2.33, the limits of the integral is set in order to avoid evanescent waves; however, it allows the existence of counter-propagating Bessel Beams. In order to prevent it, we must chose a $S(k_z)$ that mitigates or annul such contributions.

As it is going to be clear, to solve Equation 2.33, for any $S(k_z)$ we need to take it into a form of a Fourier Series. But first, we consider $S(k_z)$ a constant as expressed in Equation 2.35 below.

$$S(k_z) = \frac{c}{2\omega} \quad (2.35)$$

Thereby, solving the integral in Equation 2.33 we obtain (GRADSHTEYN; RYZHIK, 2014):

$$\Psi(x, y, z, t) = e^{-i\omega t} \text{sinc}\left(\sqrt{\frac{\omega^2}{c^2} \rho^2 + \frac{\omega^2}{c^2} z^2}\right) \quad (2.36)$$

Afterwards, we consider $S(k_z)$ as:

$$S(k_z) = \frac{c}{2\omega} e^{i2\pi n k_z / k} \quad (2.37)$$

Then, as solution, we get:

$$\Psi(x, y, z, t) = e^{-i\omega t} \text{sinc} \left(\sqrt{\frac{\omega^2}{c^2} \rho^2 + \left(\frac{\omega}{c} z + \pi n \right)^2} \right) \quad (2.38)$$

Lastly, we consider $S(k_z)$ as:

$$S(k_z) = \sum_{n=-\infty}^{\infty} A_n e^{i2\pi n k_z / K} \quad (2.39)$$

within

$$\frac{-\omega}{c} \leq k_z \leq \frac{\omega}{c} \quad (2.40)$$

where $K = 2k = 2\frac{\omega}{c}$, and A_n are the constants of the newly formulated Fourier Series expressed in Equation 2.39.

$$A_n = \frac{1}{K} \int_{-\omega/c}^{\omega/c} S(k_z) e^{i2\pi n k_z / k} dk_z \quad (2.41)$$

By looking at Equation 2.41 it can be shown that, in order to obtain the relation expressed in Equation 2.34, we can chose $A_n = \frac{1}{K} F(-2\pi n / K)$ (ZAMBONI-RACHED; RECAMI, 2008; ZAMBONI-RACHED *et al.*, 2017).

As for the solution of Equation 2.33, we have:

$$\Psi(x, y, z, t) = e^{-i\omega t} \sum_{n=-\infty}^{\infty} F\left(\frac{-2\pi n}{K}\right) \text{sinc} \left(\sqrt{\frac{\omega^2}{c^2} \rho^2 + \left(\frac{\omega}{c} z + \pi n \right)^2} \right) \quad (2.42)$$

According to (ZAMBONI-RACHED; RECAMI, 2008), this solution represents a continuous Frozen Wave and it is resistant to diffraction effects. Its spot can be calculated using Equation 2.43 below.

$$r_0 = \frac{2.4}{\sqrt{\frac{\omega^2}{c^2} - Q^2}} \quad (2.43)$$

2.2 Effect of Millimeter and Sub-Millimeter Waves in Human Body

By enhancing the fundamental knowledge of the particularities of the interaction of electromagnetic waves and biological tissues, the biological effects studies give support to the development of new bio-medical technologies and applications for electromagnetic waves. (WILMINK; GRUNDT, 2011) Biological effects studies are also responsible for health hazard evaluation and making correct and safe use of electromagnetic waves and systems.

In this section, we are going to present several concepts regarding the use, applications and thermal effects of millimeter and sub-millimeter waves. Besides, we are going to provide background concepts in biophysics and THz technology.

2.2.1 The Terahertz Region

In the Electromagnetic Spectrum, the Terahertz Region comprehends the frequency of 0.1 to 10 THz or the wavelengths ranging from 30 to 3000 μm (LIN, 2011).

In terms of energy, the Terahertz Region stands out for its photon ranging in quantum energy between 0.4 and 4.1 meV. Such energy levels is several orders of magnitude below the energy required to ionize, or remove, valence electrons from biological molecules (several eV); therefore THz radiation is classified as non-ionizing (WILMINK; GRUNDT, 2011; LIN, 2011).

Notwithstanding that THz radiation, due to its intrinsic non-ionizing feature, does not form of highly reactive free radicals, it can cause thermal effects that are indistinguishable from effects observed from bulk heating. (WILMINK; GRUNDT, 2011)

2.2.2 Terahertz-Tissue Interaction

As it happens to any other dielectric-like material, a fraction of the photon that are incident to a tissue is reflected and the remaining portion of the photons is transmitted. Mathematically, we can express the transmitted power as

$$T = 1 - R \quad (2.44)$$

where, R represent the fraction of the energy that is lost by surface reflection.

The reflection R is due to the index of refraction mismatch between the air and the

tissue, as for example, the skin. These losses can be quantified via Equation 2.45 below.

$$R = \left(\frac{n_1 - n_2}{n_1 + n_2} \right)^2 \quad (2.45)$$

As an example of the use of Equation 2.45, according to Wilmink *et al.* (2010) the optical properties of excised porcine skin have real index of refraction (n) ranging from 2.2 to 1.5 in frequencies between 0.1 and 2.0 THz. These values represent a surface reflection ranging from 15% and 9%. Furthermore, it is worthy to emphasize that the air–tissue interface leads to appreciable surface losses. (LIN, 2011)

2.2.2.1 Interaction at a Cellular Level

In general, when electromagnetic radiation penetrates skin it is rapidly absorbed by chromophores and heating occurs. According to Wilmink e Grundt (2011), many biological components of the tissues are responsible for the absorption, such as, for example, DNA, proteins and carbohydrates; however, it is a consensus in numerous researches that water is the most absorbing substance present in biological tissues, specially in millimeter and sub-millimeter wavelengths. (PAL *et al.*, 2002; PAL; ZEWAIL, 2004)

Beyond other unique properties, water has the characteristic of engaging in both inter- and intra-molecular hydrogen bonding with neighboring molecules. Such interaction results in collective vibrational modes generating heat. (LIN, 2011)

According to Welch *et al.* (2011), the absorption is responsible for the heating and the temperature rise is proportional to the total energy absorbed. The mean variation of temperature an be calculated using Equation 2.46 below.

$$\Delta T = \frac{\mu_a H}{\rho c} \quad (2.46)$$

where, in this case, c represents the heat capacity and ρ is the density of the tissue. The total ρc is estimated, for tissues, to be around $4.2 J \text{ cm}^{-3} \text{ } ^\circ C^{-1}$. Besides, H is the radiant exposure measured in $J \text{ cm}^{-2}$.

It is important to point out that when dealing with such distinct fields, as optics and heat transfer, there are several duplication of symbols

2.2.3 Thermal Energy Induced in Tissues by Electromagnetic Waves

So far, we know that laser irradiated tissue responds with a fully dissipative process of absorbing photons and increasing its temperature. Furthermore, in conjunction with this

effect, there will be a diffusion of heat to surrounding areas that are cooler. (WELCH *et al.*, 2011) Hence, it is necessary to make a careful analysis of the processes and consequences related to applying electromagnetic waves in biological tissues.

But first, we need to evaluate the amount of energy that is deposited into the tissue. This calculation is the rate of heat generation and is defined in Equation 2.47 below.

$$S(r, z) = \mu_a(r, z)\Phi_0(r, z) \quad (2.47)$$

where $\mu_a(r, z)$ is the material absorption coefficient at a given point; and $\Phi_0(r, z)$ is the irradiance at some point in the tissue measured in (W/m²).

Using Equation 2.47, it is possible to evaluate, for any arbitrary location, the temperature rise (K) as shown in Equation 2.48

$$\Delta T(r, z) = \frac{S(r, z)\Delta t}{\rho c} \quad (2.48)$$

where, Δt is the time of exposition to the electromagnetic radiation; ρ is the density of the tissue (g/m³); and, c is the specific heat of the tissue (J/g°K).

As stated before, we need to be careful and take in account all the processes of heat transfer. So far, we have acquainted only the irradiation form of heat transfer. However, when heating a specific local a heat gradient will form and try to dissipate the thermal energy to surrounding areas (conduction process). In addition to that, in biological tissues, there will be heat spreading because of the blood that is perfused through the vascular network. According to Welch *et al.* (2011), the arterial network is very specific for each type of tissue and has a unique geometry. This feature results in a convection process that interfere in the total energy of the system.

According to Lin (2011), the conduction driven by a temperature gradient can be described by Fourier's Law.

$$q_{cond} = -kA \frac{\Delta T}{\Delta X} \quad (2.49)$$

where, q_{cond} is the heat flux in (W), A is the area of the irradiated tissue, k is the thermal conductivity, and $\frac{\Delta T}{\Delta X}$ is the temperature gradient in the direction of the heat flow.

Besides, according to Welch *et al.* (2011), the convection process occur when a solid material is in contact with a fluid at a different temperature. In the biological case, the irradiated tissue is in a different temperature than the blood that passes through the veins and

arteries. In order to calculate the amount of heat exchanged by convection we use Newton's law of cooling, described in Equation 2.50 below.

$$q''_{conv} = h(T_s - T_a) \quad (2.50)$$

where, T_s is the tissue temperature, T_a is the surrounding temperature, q''_{conv} is the heat flux in (W/m^2), and h is the convective coefficient ($W/m^2\text{K}$).

The convective coefficient is the hardest part to acquaint in Equation 2.50 because there exists four distinguishing characteristics that alter the intensity of the convection process. (WELCH *et al.*, 2011)

Lastly, for completeness, we can assess the heat transport arising from the spontaneous emission of EM waves by matter, so-called Radiative. (LIN, 2011) This process is described by Stefan–Boltzmann's law, as follows:

$$q_{rad} = \sigma\epsilon(T_S^4 - T_a^4) \quad (2.51)$$

where q_{rad} is the heat flux in (W); σ is the Stefan–Boltzmann constant $5.670 \times 10^{-8} \text{ J m}^{-2} \text{ K}^{-4} \text{ s}^{-1}$; and, ϵ is the emissivity.

2.2.3.1 Thermal Damage to Cells and Tissues

When a biological tissue is submitted to heat the kinetic energy of the molecules are increased generating a temperature rise. And, if the kinetic energy of the molecules becomes greater than the intramolecular bounds the tissue starts to deteriorate. (LIN, 2011)

In general, the thermal effects on tissues are divided into three categories: low temperature ($43^\circ\text{C} - 100^\circ\text{C}$) middle temperature zone ($100^\circ\text{C} - 300^\circ\text{C}$), and high temperature zone ($300^\circ\text{C} - 1000^\circ\text{C}$). In general, most modern electromagnetic sources do not have enough power to induce temperature rises to provoke middle or high temperature zones. Therefore the study of the thermal effects on the low temperature zone is the most relevant for this work.

A spatiotemporal temperature increase can provoke several damage to the tissue. At the cellular level, damage includes - but not limited to - cellular membrane deformation, DNA damage, death via necrotic mechanisms.

The amount of time in which the tissue is exposed to high temperatures drives the amount and gravity of the damage. Research suggests that the point of cellular death can be

achieved with a temperature of 45°C for 30 min. More specific data can be found in (WELCH *et al.*, 2011).

3 Generation of Beams Truncated by Finite Apertures in Millimeter and Sub-millimeter Wavelengths

It is well known the importance of studying wave beams to establish an analytic description of their propagation. As a result of that, many works have been done in the characterization of different beams, especially in optical frequencies.

An example of these works includes (GORI *et al.*, 1987), in which a Bessel beam is apodized by a Gaussian function; and, therefore it can become an experimentally realizable version of a Bessel Beam with finite energy, the Bessel-Gauss beam.

Despite the existence of works describing finite energy Bessel beams, most of them still meet mathematical difficulties and requires numerical simulations. These difficulties are even more evident when one tries to describe beams in GHz and THz range of frequencies and/or to describe waves truncated by finite apertures.

As for the truncated beams, there are rare works, mainly based on the Fresnel Diffraction Integral, describing their behavior. One of the best examples is presented in (WEN; BREAZEALE, 1988), in which superposition of Gaussian beams described axially symmetrical beams truncated by circular apertures. The method requires the calculation of superposition coefficients; and, in order to do that, it is necessary to adopt computational optimization processes. There were some attempts to simplify this method, as presented in (DING; ZHANG, 2004).

To deal with the mathematical difficulties present on the previous methods, Zamboni-Rached, Recami, and Balma developed a simple and effective method to describe some important wave beams truncated by finite apertures. (ZAMBONI-RACHED *et al.*, 2012) In this method, important truncated beams can be obtained by means of Bessel-Gauss beam superposition, whose coefficients are found in a straightforward manner.

In this chapter we use the method proposed in (ZAMBONI-RACHED *et al.*, 2012) to yield scalar and vectorial analytical solutions to plane waves, Gauss, Bessel-Gauss, and Bessel beams truncated by circular apertures in GHz and THz frequencies.

3.1 Scalar Approach

We start with the Fresnel Diffraction Integral in cylindrical coordinates, assuming azimuthal symmetry, presented on Equation 3.1. This equation is used to yield the paraxial solution for a monochromatic scalar wave field when knowing its shape on the plane $z = 0$.

It should be noticed that we are assuming and suppressing a time dependency of the kind $\exp(-i\omega t)$.

$$\Psi(\rho, z) = \frac{-ik}{z} \exp \left[i \left(kz + \frac{k\rho^2}{2z} \right) \right] \int_0^\infty \psi(\rho', 0) \exp \left(ik \frac{\rho'^2}{2z} \right) J_0 \left(k \frac{\rho\rho'}{z} \right) \rho' d\rho' \quad (3.1)$$

where k is the wavenumber, λ is the wavelength, and $\psi(\rho', 0)$ indicates the field on $z = 0$ (the excitation field).

Using Equation 3.1 one can yield a Bessel-Gauss beam by choosing as excitation the following pattern.

$$\psi(\rho', 0) = AJ_0(k_\rho \rho') \exp(-q\rho'^2) \quad (3.2)$$

By applying Equation 3.2 in 3.1 we get the so-called Bessel–Gauss beam given by:

$$\Psi_{BG}(\rho, z) = -\frac{ikA}{2zQ} \exp \left[i \left(kz + \frac{\rho^2 k}{2z} - \omega t \right) \right] J_0 \left(\frac{ik k_\rho \rho}{2zQ} \right) \exp \left[-\frac{1}{4Q} \left(k_\rho^2 + \frac{k^2 \rho^2}{z^2} \right) \right] \quad (3.3)$$

where k_ρ is the transverse wavenumber and $Q = q - \frac{ik}{2z}$.

The result obtained in Equation 3.3 is one of the few solutions to the Fresnel diffraction integral that can be obtained analytically. In this particular case, we are considering a Bessel beam apodized by a Gaussian function. For a beam truncated by finite aperture of radio R , finding such solution becomes rather complicated because the upper limit of the integral becomes R ; which, in general, ends up requiring lengthy numerical calculations.

However, if we consider the solution obtained in Equation 3.3, and apply linearity property, we can write the following solution to the Fresnel diffraction integral:

$$\Psi(\rho, z) = \exp(ikz)\psi(\rho, z) \quad (3.4)$$

with:

$$\psi(\rho, z) = -\frac{ik}{2z} \exp\left(\frac{i\rho^2 k}{2z}\right) \sum_{n=-N}^N \frac{A_n}{Q_n} J_0\left(\frac{ik k_\rho \rho}{2z Q_n}\right) \exp\left[-\frac{1}{4Q_n} \left(k_\rho^2 + \frac{k^2 \rho^2}{z^2}\right)\right] \quad (3.5)$$

where A_n are still unknown constants, and Q_n are chosen as:

$$Q_n = q_n - ik/2z \quad (3.6)$$

In Equation 3.6, q_n is a constant that *can assume complex values* and it is chosen as:

$$q_n = q_R - i \frac{2\pi n}{L} \quad (3.7)$$

where q_R and L are constants with the dimensions of a square length.

Moreover, the initial field (i.e., at $z = 0$) for this superposition of beams is given by:

$$\Psi(\rho, 0) = J_0(k_\rho \rho) \sum_{n=-\infty}^{\infty} A_n e^{-q_n \rho^2} \quad (3.8)$$

Applying Equation 3.7 into Equation 3.8, we obtain:

$$\Psi(\rho, 0) = J_0(k_\rho \rho) e^{-q_R \rho^2} \sum_{n=-\infty}^{\infty} A_n e^{\frac{i2\pi n \rho^2}{L}} \quad (3.9)$$

What we are going to show, according to (ZAMBONI-RACHED *et al.*, 2012), is that solution 3.5 can be used to represent (describe) important beams truncated by finite apertures of radius R . More specifically, we are interested in the excitations, on the plane $z = 0$, presented on Table 1.

Table 1 – Initial field excitation for important particular cases of localized waves

Excitation Type	Equation
Truncated Plane Wave	$\psi_{TP}(\rho, 0) = \text{circ}\left(\frac{\rho}{R}\right)$
Truncated Gaussian Beam	$\psi_{TG}(\rho, 0) = e^{-q\rho^2} \text{circ}\left(\frac{\rho}{R}\right)$
Truncated Bessel Beam	$\psi_{TB}(\rho, 0) = J_0(k_\rho \rho) \text{circ}\left(\frac{\rho}{R}\right)$
Truncated Bessel-Gauss Beam	$\psi_{TBG}(\rho, 0) = J_0(k_\rho \rho) e^{-q\rho^2} \text{circ}\left(\frac{\rho}{R}\right)$

Thus, in order to achieve our goal, given a beam truncated by an aperture of radius R at $z = 0$, we have to determine values of A_n , q_R and L that make Equation 3.9 represent with fidelity the excitation signals listed on Table 1.

It is natural that, in the cases of Truncated Bessel Beams and Truncated Bessel-Gauss Beams, the quantity k_ρ be set as the beam transverse wavenumber. And, for the Truncated Plane Wave or the Truncated Gauss Beam, this quantity must be equal to zero.

Besides, for all cases the function

$$\exp(-q_R \rho^2) \sum_{n=-\infty}^{\infty} A_n \exp\left(i \frac{2\pi n}{L} \rho^2\right) \quad (3.10)$$

must be approximately equal to $\exp(q\rho^2) \text{circ}(\frac{\rho}{R})$.

Let us now prove that it is possible. Toward such goal, we suppose a function $G(r)$.

$$G(r) = \begin{cases} e^{qRr} e^{-qr} & \text{for } |r| \leq R^2 \\ 0 & \text{for } R^2 < |r| < L/2 \end{cases} \quad (3.11)$$

where q is a constant.

The function $G(r)$ can be expanded in a Fourier Series:

$$G(r) = \sum_{n=-\infty}^{\infty} A_n e^{\frac{i2\pi nr}{L}} \quad (3.12)$$

where $|r| \leq L/2$, and it is simple to show that:

$$A_n = \frac{1}{L(q_R - q) - i2\pi n} \left\{ \exp\left[\left(q_R - q - \frac{i2\pi n}{L}\right)R^2\right] - \exp\left[-\left(q_R - q - \frac{i2\pi n}{L}\right)R^2\right] \right\} \quad (3.13)$$

At this point, by writing $r = \rho^2$ in Equation 3.11 and 3.12 the product given in 3.10 can be written as:

$$\exp(-q_R \rho^2) \sum_{n=-N}^N A_n \exp\left(i \frac{2\pi n}{L} \rho^2\right) = \begin{cases} e^{-q\rho^2} & \text{for } |\rho| \leq R \\ 0 & \text{for } R < |\rho| < \sqrt{L/2} \\ e^{-q_R \rho^2} G(\rho^2) \approx 0 & \text{for } |\rho| > \sqrt{L/2} \end{cases} \quad (3.14)$$

where A_n are given by Equation 3.13 and $G(\rho^2)$, given by Equation 3.12 (with $r = \rho^2$), is a function that, according to Equation 3.11 possesses maximum values given by $e^{(q_R - q)R^2}$ (if

$q_R > q$) or 1 (if $q_R < q$) for $\rho > \sqrt{L/2}$. Since $\sqrt{L/2} > R$, it is always possible to choose q_R and L values that make $e^{-q_R \rho^2} G(\rho^2) \approx 0$ for $\rho \geq \sqrt{L/2}$. Mathematically, we must have:

$$e^{-q_R \rho^2} G(\rho^2) \ll 1 \quad (3.15)$$

for $\rho > \sqrt{L/2}$.

That implies in:

$$e^{-q_R L/2} e^{(q_R - q)R^2} \ll 1, \text{ for } q_R > q \quad (3.16)$$

and, for $q_R < q$:

$$e^{-q_R L/2} \ll 1 \quad (3.17)$$

Equations 4.8 and 4.9 are the criteria that must be used when choosing q_R and L .

Therefore, Equation 3.9 can be used to represent the Truncated Beams in Table 1, in which the A_n coefficients are given by Equation 3.13 with q_R and L adequately chosen according to the criteria set by Equations 4.8 or 4.9. This way, the resulting field emanating from the circular aperture of radius R in $z = 0$ is given by Equation 3.5.

3.2 Ensuring the Validity of the Scalar Approach

It has been seen in (ZAMBONI-RACHED *et al.*, 2012) that the scalar method gives a good representation for the field propagation in several situations; however, in cases where the beam is relatively non-paraxial this method can not be used. In such cases, we need to considerate the vectorial nature of the field.

In order to solve this problem, we can assume an Electric Field given by:

$$\vec{E} = E_y \hat{y} + E_z \hat{z} \quad (3.18)$$

and we suggest that the field component along the \hat{y} direction (E_y) is equal to the scalar field given by Equation 3.5.

To find the axial component E_z of the electric field solution we consider a free-space propagation and apply Gauss's Law ($\nabla \cdot \vec{E} = 0$):

$$E_z = - \int \frac{\partial E_y}{\partial y} dz \quad (3.19)$$

Analysing Equation 3.19, it is clear that the partial derivative can be taken out of the integral. By that means, we now represent Equation 3.19 as:

$$E_z = - \frac{\partial}{\partial y} \int e^{ikz} \psi(x, y, z) dz \quad (3.20)$$

where $\psi(x, y, z)$ is the envelop given by Equation 3.5.

Now we assume that e^{ikz} varies much faster than the envelop. So that:

$$E_z \approx \frac{-\partial \psi(x, y, z)}{\partial y} \int e^{ikz} dz \quad (3.21)$$

which results in:

$$E_z \approx ie^{-i\omega t} \frac{e^{ikz}}{k} \frac{\partial \psi(x, y, z)}{\partial y} \quad (3.22)$$

Lastly, notice that $|E_z| \approx |\frac{\partial E_y}{\partial y}| \frac{1}{k}$; also, the paraxial approximation suggests that the variation of the envelop is much smaller than $\exp(ikz)$. Therefore, $|E_z|$ is much less $|E_y|$ for the paraxial regime; and, in these cases $\vec{E} \approx E_y \hat{y}$, justifying the scalar approach.

3.3 Results and Discussions

In this section we shall apply our descriptions for the beams in submillimeter and millimeter wavelengths.

3.3.1 Analytic Description of the Truncated Plane Wave

We start by a plane wave whose initial excitation is represented by $\Psi_{TP}(\rho, 0) = \text{circ}(\rho/R)$. This initial field configuration can be modeled by Equation 3.9 by considering $k_\rho = q = 0$. For this configuration we adopt $L = 4R^2$ and $q_R = 6/L$; values that satisfy equation 3.14. Beyond that, in order to perform the simulation on MATLAB, we choose $f = 50$ GHz, $N = 60$, and $R = 1$ 0cm. By that means, Figure 5 shows the initial field at $z = 0$; and, the resulting field emanated by the finite aperture.

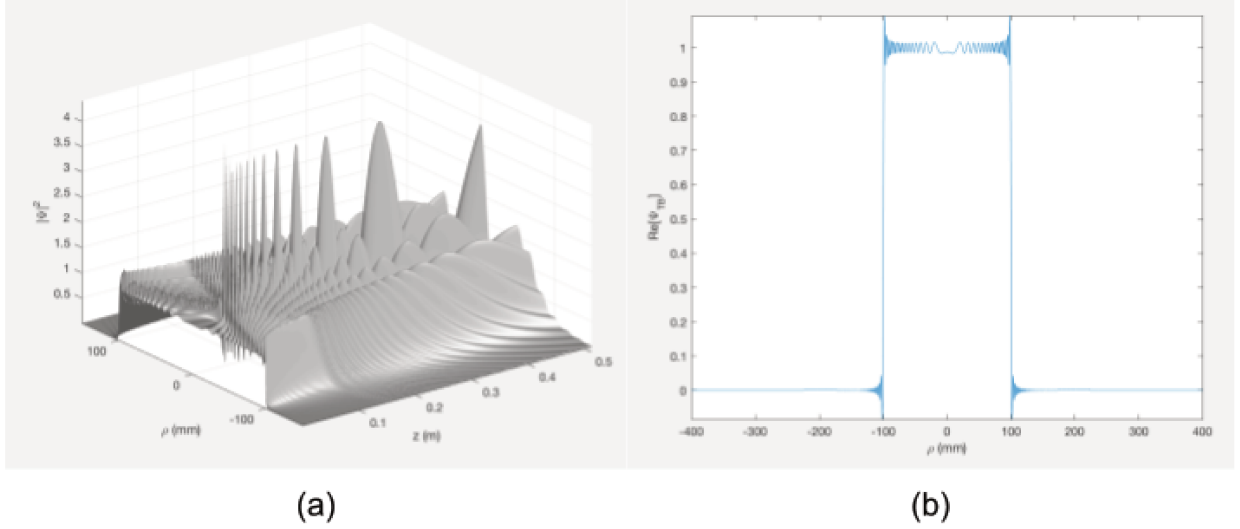


Figure 5 – a) Emanating field for a 50 GHz circularly truncated plane wave. b) Initial field for a 50 GHz truncated plane wave with $R = 10$ cm.

3.3.2 Analytic Description of the Truncated Gauss Beam

Let us now consider a truncated Gauss beam whose truncating circular aperture has a radius of $R = 5$ cm. Its excitation signal at $z = 0$ is represented by $\Psi_{TG}(\rho, 0) = e^{-q\rho^2} \text{circ}(\rho/R)$. This initial field configuration can be modeled by Equation 3.9 by considering $k_\rho = 0$. For this configuration we adopt $L = 4R^2$ and $q_R = 8/L$; values that satisfy equation 3.14. Beyond that, in order to perform the simulation, we choose $f = 100$ GHz, $N = 100$, and $q = 300$. Thereby, Figure 6 shows the initial field at $z = 0$. The resulting field emanated by the finite aperture is shown in Figure 6.

3.3.3 Analytic Description of the Truncated Bessel-Gauss Beam

Subsequently, let us consider a Truncated Bessel-Gauss Beam at the frequency of 200 GHz. Its excitation signal at $z = 0$ applied to Equation 3.1 is $\Psi_{TBG}(\rho, 0) = J_0(k_\rho \rho) e^{-q\rho^2} \text{circ}(\rho/R)$; and, it is obtained via Equation 3.9. For this configuration we adopt $L = 10R^2$ and $q_R = q$, $R = 10$ cm, and $N = 25$; values that satisfy Equation 3.14. By that means, Figure 7 shows the initial field at $z = 0$; and, the resulting field emanated by the finite aperture.

3.3.4 Analytic Description of the Truncated Bessel Beam

Lastly, we wish to simulate a Bessel Beam at the frequency of 300 GHz. The excitation signal for a Truncated Bessel Beam is represented by $\Psi_{TB}(\rho, 0) = J_0(k_\rho \rho) \text{circ}(\rho/R)$. This initial field configuration can be modeled by Equation 3.9 by considering $q = 0$. For this

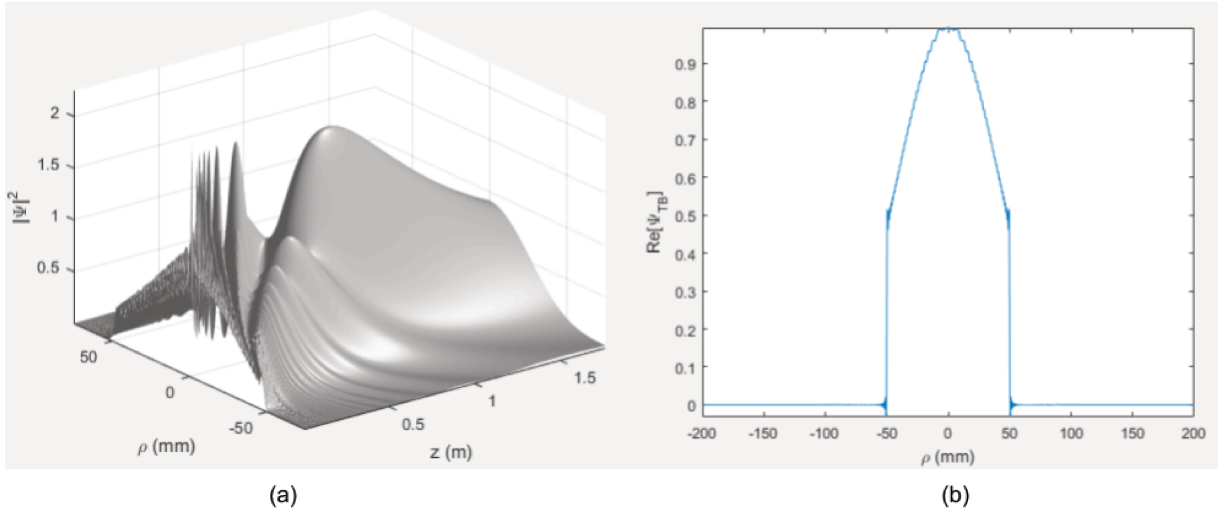


Figure 6 – a) Emanating field for a 100 GHz circularly truncated Gauss beam. b) Initial field for a 100 GHz truncated Gauss beam with $R = 5$ cm.

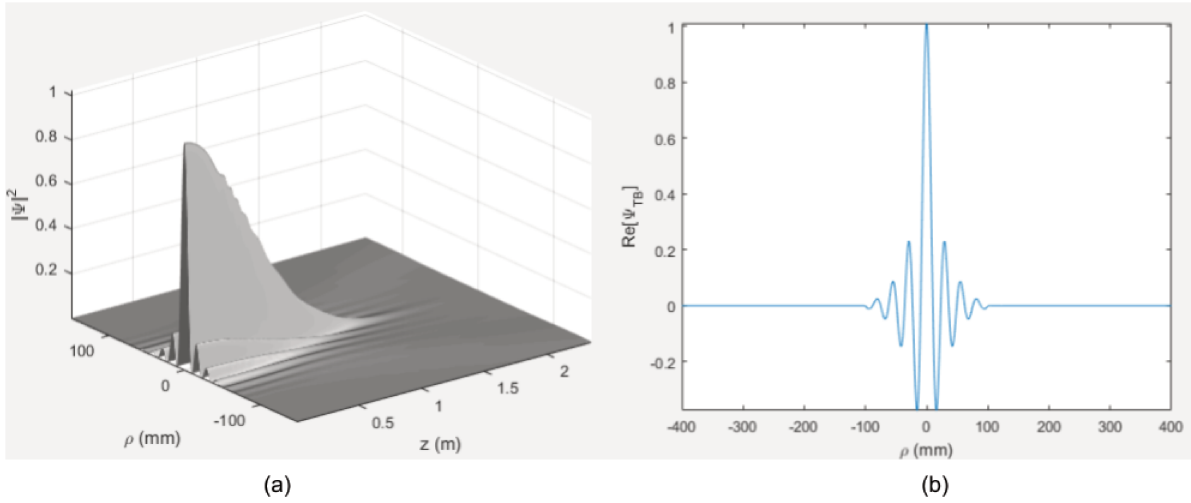


Figure 7 – a) Emanating field for a 200 GHz truncated Bessel-Gauss beam. b) Initial field for a 200 GHz truncated Bessel-Gauss beam with $R = 10$ cm.

configuration we adopt $L = 4R^2$ and $q_R = 5/L$; values that satisfy Equation 3.14. Beyond that, in order to perform the simulation, we choose $N = 23$, $R = 15$ cm, and the transverse wavenumber $k_\rho = 959.94$, which corresponds to a beam spot with radius approximately equal to $\Delta_\rho = 2.5$ mm. By that means, Figure 8 shows the initial field at $z = 0$; and, the resulting field emanated by the finite aperture.

Truncated Beam description and analysis is an important research field due to its applicability in various scenarios; for instance, in (ZAMBONI-RACHED; RECAMI, 2014) this method was used to design a circularly polarized RLSA Antenna to generate a Truncated

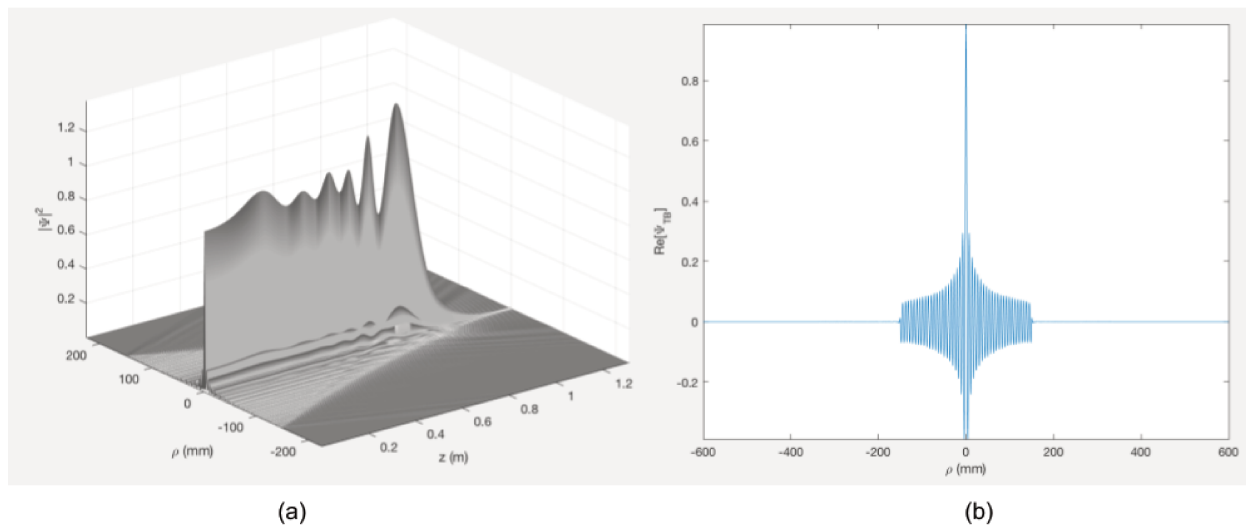


Figure 8 – a) Emanating field for a 300 GHz circularly truncated Bessel beam. b) Initial field for a 300 GHz truncated Bessel beam with $R = 15$ cm.

Bessel Beam at 15 GHz of frequency. Later on, this antenna, on board of a vehicle, was used to detect buried objects.

Besides, according to (LIN, 2011), THz waves are suitable to provide temperature rise to tissues; and, later in this thesis, we shall evaluate the possibility of using them within the human body. We expect to use this characterization to propose structures capable of generating such beams. We envision this work being used to induce hyperthermic effects on human body; since hyperthermia has been reported as a form of cancer treatment in many papers in literature. (SHELLMAN *et al.*, 2008)

4 Generation of Bessel Beams: A Redesign of an Antenna Model

4.1 Introduction

At optical frequencies, Bessel Beams can be generated in different ways, for example, we can cite Durnin's experiment (DURNIN *et al.*, 1987) which was the first known method for generating Bessel Beams. This method was able to generate a propagating Bessel Beam using a laser source focusing over an annular slit positioned at the focus of a convex lens; and the resulting beam was able to travel about 85 cm keeping its transverse intensity shape approximately unchanged. As a more recent example of Bessel Beam launcher we can cite axicon-based generation (MONK *et al.*, 1999; ARLT; DHOLAKIA, 2000), and holography-based (using spatial light modulator) (CHATTRAPIBAN *et al.*, 2003; MCGLOIN; DHOLAKIA, 2005).

Unfortunately, none of the aforementioned methods can be used (some at least not with the same simplicity) in the generation of Bessel Beams in GHz; therefore, we will focus our attention on Bessel Beam launchers developed to operate at such wavelengths.

After a thorough analysis of the methods that have been proposed previously, we decided to focus our attention on a *Radial Slot Array Antenna* (RLSA Antenna). The reason for this choice are the multiple advantages that comes with it, such as being low-profile, planar, single-layer, and simply fed in a single point at the center of the antenna (MAZZINGHI *et al.*, 2014).

In this chapter we aim to use the existing of Leaky Wave Antennas and Bessel Beam generation (see (LEMAÎTRE-AUGER *et al.*, 2011; FUSCALDO, 2017; FUSCALDO *et al.*, 2018) and references therein) to design a new antenna working in a different frequency. Also, we shall assess the effects of one of the antenna dimensions in its radiating pattern.

This chapter is divided into 4 parts. In section 4.2, we establish the foundations for the design of the model; and, we perform an field evaluation of the aperture antenna. Afterwards, in section 4.3 we propose a model with a set of physical dimensions and operating characteristics. The simulated results are presented in section 4.4 and further investigation are developed in section 4.5.

4.2 Design Foundation and Field Evaluation

The design of the antenna here considered for generation of Bessel Beams takes into account a dielectric filled Parallel Plate Waveguide (PPW) whose upper plate consists in a metal with annular slits carved within, here denominated as Metallic Strip Grating (MSG). The main idea for this model is to have a Bessel pattern in the transverse plane inside the cavity; and, by properly choosing slits widths (w_s) and positions (ρ_s) to make this pattern leak out to free space. Such structure is presented in (ALBANI *et al.*, 2014) and can be seen in Figure 9. Note that, in the figure, the z axis is pointing out of the antenna surface.

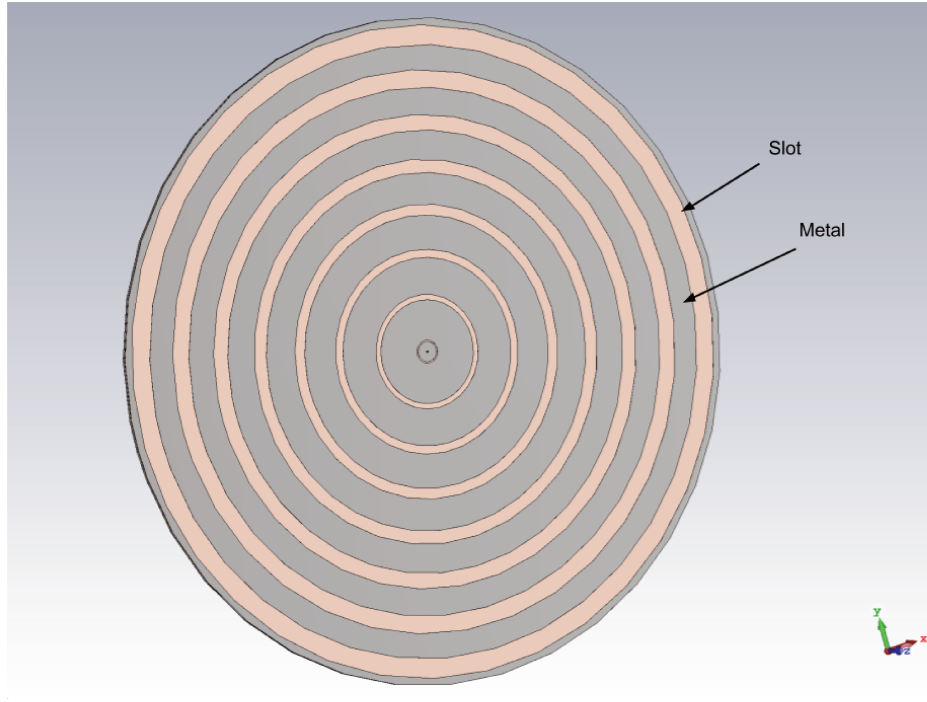


Figure 9 – Top view of a dielectric filled PPW with slit grating. Each slit has a width w_s and its center is positioned in relation to the center of the antenna from a distance ρ_s

In order to attest the capability of this structure to radiate an Bessel Beam in its near field, we need to perform a field evaluation in the region inside the waveguide. We consider this PPW as having a metallic rim at its external border and being excited by a coaxial feed at its center inducing an outward cylindrical radial wave.

Due to the placement of the metallic wall, an outward and inward leaky wave propagates inside the structure giving rise to a resonant leaky wave. (FUSCALDO, 2017)

Since we are aiming for a Transverse Magnetic (TM) Bessel Beam, we search for solutions with $E_z(\rho, 0) = J_0(k_\rho \rho) e^{-ik_z z} e^{i\omega t}$. Naturally, a z-component only Magnetic Vec-

tor Potential can be used to derive all the field components. Therefore, we start from the homogeneous Helmholtz equation in cylindrical coordinates:

$$\frac{\partial^2 A_z}{\partial \rho^2} + \frac{1}{\rho} \frac{\partial A_z}{\partial \rho} + \frac{1}{\rho^2} \frac{\partial^2 A_z}{\partial \phi^2} + \frac{\partial^2 A_z}{\partial z^2} + k^2 A_z = 0 \quad (4.1)$$

And, from this point, one can find a generic solution (presented in Equation 4.2) for the Magnetic Vector Potential inside this cylindrical waveguide.

$$A_z = \cos(k_z z) e^{-in\phi} [A_1 H_n^{(1)}(k_\rho \rho) + A_2 H_n^{(2)}(k_\rho \rho)] \quad (4.2)$$

where $k_z^2 + k_\rho^2 = k^2$.

Assuming an ϕ -invariant field ($\frac{\partial}{\partial \phi} = 0$), we have $n = 0$ and Equation 4.2 reduces to:

$$A_z = \cos(k_z z) [A_1 H_0^{(1)}(k_\rho \rho) + A_2 H_0^{(2)}(k_\rho \rho)] \quad (4.3)$$

We can derive expressions to the magnetic field by using $\vec{B} = \nabla \times \vec{A}$; which, consequently, leads to $E_\phi = H_\rho = H_z = 0$, due to the azimuthal characteristic of the fields, and

$$E_\rho = i \frac{\eta k_z k_\rho}{k} \sin(k_z z) [A_1 H_1^{(1)}(k_\rho \rho) + A_2 H_1^{(2)}(k_\rho \rho)] \quad (4.4)$$

$$E_z = i \frac{\eta k_\rho^2}{k} \cos(k_z z) [A_1 H_0^{(1)}(k_\rho \rho) + A_2 H_0^{(2)}(k_\rho \rho)] \quad (4.5)$$

$$H_\phi = k_\rho \cos(k_z z) [A_1 H_1^{(1)}(k_\rho \rho) + A_2 H_1^{(2)}(k_\rho \rho)] \quad (4.6)$$

It is noticeable in Equations 4.4, 4.5, and 4.6 that the fields are represented as a superposition of two Hankel functions (one outward and the other one inward). The goal here is to obtain a Bessel-like pattern for E_z . For that reason, we will need to make $A_1 \approx A_2$ by placing a metallic rim at a distance $\rho = \rho_B$ which corresponds to one of the zeros of the Bessel function $J_0(k_\rho \rho)$. Therefore, we will have $E_z = 0$ at $\rho = \rho_B$; and, consequently, we have:

$$A_1 H_0^{(1)}(k_\rho \rho) = -A_2 H_0^{(2)}(k_\rho \rho) , \quad (4.7)$$

from where we can extract an expression for A_1 as being:

$$A_1 = \frac{-A_2 H_0^{(2)}(k_\rho \rho)}{H_0^{(1)}(k_\rho \rho)} \quad (4.8)$$

Supposing a value of ρ_B sufficiently large (to allow several oscillations), and recalling that for an open waveguide structure, as the one under consideration, complex waves emerge as general source-free solutions (TAMIR; OLINER, 1963) k_ρ is defined as

$$k_\rho = \beta_\rho + i\alpha_\rho \quad (4.9)$$

the Hankel Functions can be approximated as:

$$H_0^{(1),(2)} \approx \sqrt{\frac{2}{\pi k_\rho \rho}} \exp \left[-i \left(k_\rho \rho - \frac{\pi}{4} \right) \right] \quad (4.10)$$

Using Equation 4.10 in Equation 4.8 we obtain:

$$A_1 = -A_2 \exp(2\alpha_\rho \rho_B) \exp[2i(\beta_\rho \rho_B - \pi/4)] \quad (4.11)$$

Thus, the conditions in order to make $A_1 \approx A_2$ are presented in Equations 4.12 and 4.13.

$$\alpha_\rho \rho_B \ll 1 \quad (4.12)$$

$$\beta_\rho \rho_B = \frac{\pi}{4} + q\pi \quad (4.13)$$

where $q \in \mathbb{Z}$.

These equations tell us that, in order to obtain a zeroth-order Bessel function, the inward and backward Hankel functions must have nearly identical amplitude and they must be out of phase.

At this point, to fully derive the fields, we need to evaluate the coefficient A_2 . Therefore, we need to take into consideration the type of excitation used. In this case, we want to use a coaxial excitation that induces a current I given by:

$$I = 2\pi a J_s \quad (4.14)$$

where a is the radius of the internal conductor, and J_s is a constant current distribution (at these frequencies penetration depth is minimal).

Assuming a very thin wave-guide ($h \ll \lambda_0$, where h is the height of the dielectric slab and λ_0 the vacuum wavelength of the operating frequency) it is possible to use boundary condition on H_ϕ to determine A_2 . That said, at $z = 0$ the current density can be found by applying Ampère-Maxwell's Law.

$$k_\rho[A_1 H_1^{(1)}(k_\rho a) + A_2 H_1^{(2)}(k_\rho a)] = J_s \quad (4.15)$$

Assuming a very small, we can use small argument approximations for Hankel functions and obtain:

$$A_2 = \frac{-I}{4i} + A_1 \quad (4.16)$$

Now, we can finally write expressions for E_ρ , E_z , and H_ϕ which uniquely describe the fields inside the wave-guide.

$$E_\rho = i \frac{A_1 \eta k_z k_\rho}{k} \sin(k_z z) J_1(k_\rho \rho) \quad (4.17)$$

$$E_z = i \frac{A_1 \eta k_\rho^2}{k} \cos(k_z z) J_0(k_\rho \rho) \quad (4.18)$$

$$H_\phi = A_1 k_\rho \cos(k_z z) J_1(k_\rho \rho) \quad (4.19)$$

It is noticeable that, unlike what we wanted, Equation 4.18 has a cosinusoidal dependency. However, let us remember that we are dealing with fields that are confined within the wave-guide. By having the bottom plate at $z = 0$, the top plate is located at a height $z = h$; hence, we shall have the constant $\cos(k_z h)$ as part of Equation 4.18 resulting in the desired z -invariant Bessel function.

Also, since there are metallic walls confining these fields, the tangential electric field to the top and bottom plates E_ρ must be equal to zero; therefore we must have:

$$k_z h = n\pi \quad (4.20)$$

In conclusion, regardless of the simplicity of the model, the antenna can indeed support the generation of a Bessel Beam resulting from the superposition of outward and inward Hankel waves. (COMITE *et al.*, 2018)

4.3 Antenna Proposal

Since we know that the antenna presented in Figure 9 can reproduce approximately a Bessel pattern on its initial plan; in this section, we aim to define a set of physical parameters for its construction.

Firstly, by using Ray-Optics we can interpret how fields propagates, emanates and/or radiates from the antenna. According to Figure 10, when the antenna is fed in a single point at its center, an outward wave starts to propagate within the waveguide. Due to the Metallic Strip Grating (MSG), the propagating fields are able to leak, as indicated by the green arrows on Figure 10. This leakage is characteristic of an open waveguide as predicted by (TAMIR; OLINER, 1963); and, consequently, they are related to the propagating complex wave that emerge as a general solution the this kind of problem. These waves have a complex radial wave number k_ρ described by Equation 4.9.

The imaginary part α_ρ can be seen as an attenuation coefficient that, even though it accounts for losses in the material, mainly describes the amount of energy leaked in form of radiated power. In addition, this type of open waveguide structures with complex wave as solutions are often referred to as *leaky waves antennas*. (TAMIR; OLINER, 1963)

It should be noted that, in this paper, we chose to work solely with the so-called *physical leaky waves* which are complex waves that attenuate as they propagate and have positive imaginary part of the radial wave number ($\alpha_\rho > 0$). (FUSCALDO *et al.*, 2018)

Thereafter, when the outward waves reach the metallic rim at the extremity of the antenna it is reflected arising an inward wave whose leaked fields are pointed towards the z-axis (see blue arrows on Figure 11). Due to the azimuthal nature of the antenna, this backward radiation overlaps and generate a focused Bessel Beam on the light blue region of Figure 11 close to the axis of symmetry. Outside that region, spurious unfocused radiation envelopes the central focused beam. (FUSCALDO *et al.*, 2018)

As it can be seen in Figure 11, the structure and its radiated fields are azimuthally invariant. Furthermore, as it has been mentioned before, the truncation of the aperture limits the beam propagation distance. Such limited range of propagation is commonly referred as *Non-diffracting range* and can be calculated via Equation 2.22.

Besides, at this point, we would like to introduce the fact that the structure under consideration has a periodic Metallic Strip Grating (MSG) along the radial direction ρ ; such feature can be seen better in Figure 12.

By all means, when a MSG is etched in a Parallel Plate Waveguide it can be seen as a wave perturbation and it results in Leaky Waves achieved by an axially fast spatial

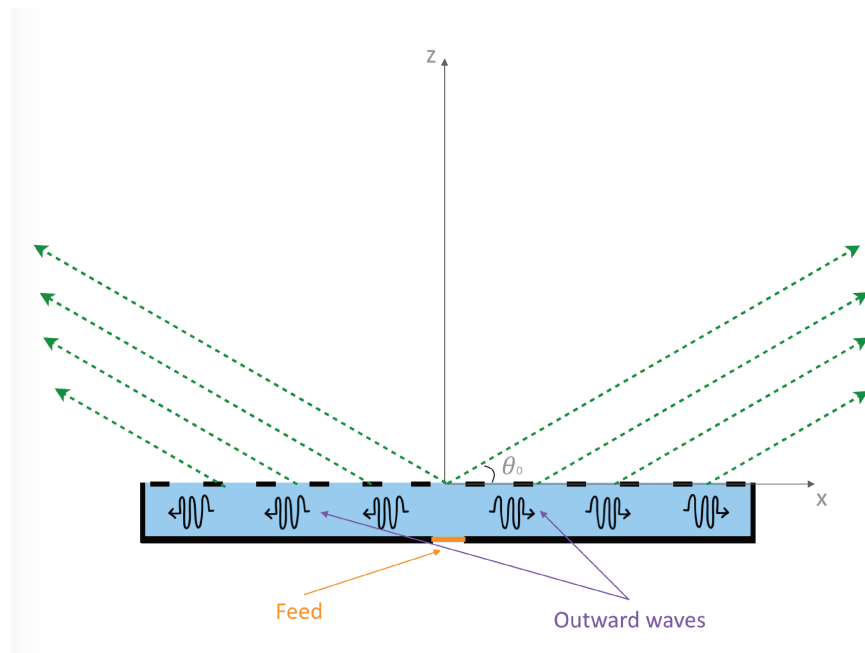


Figure 10 – Cross-sectional view of the proposed structure. The green arrows represent the fields that are leaking away from the antenna as the outward waves propagates.

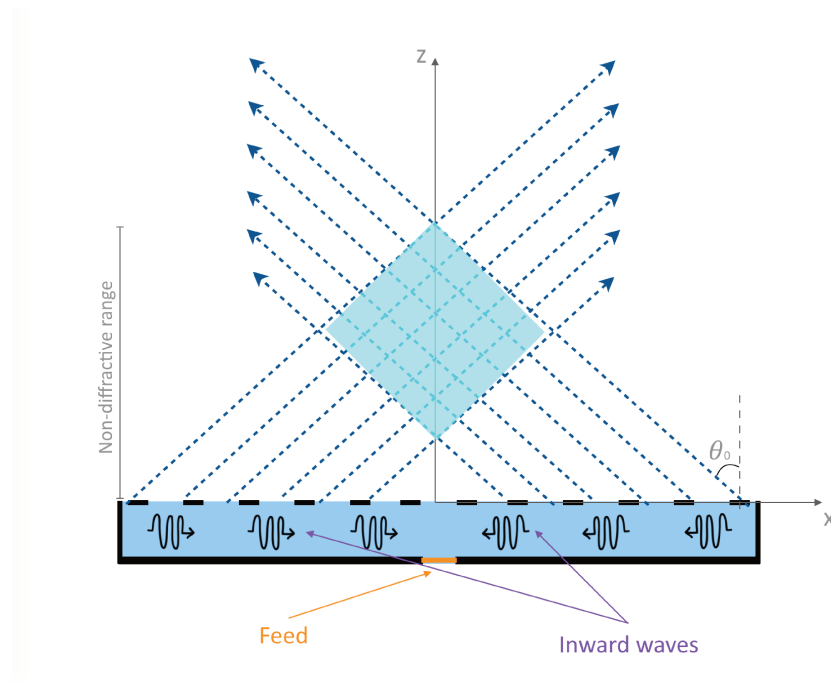


Figure 11 – Cross-sectional view of the proposed dielectric filled PPW. The light blue diamond shape represents the spatial region in which the Bessel Beam is formed as a result of interference of the leaked field.

harmonic. (PODILCHAK *et al.*, 2014) Therefore, the structure can be defined by a strip

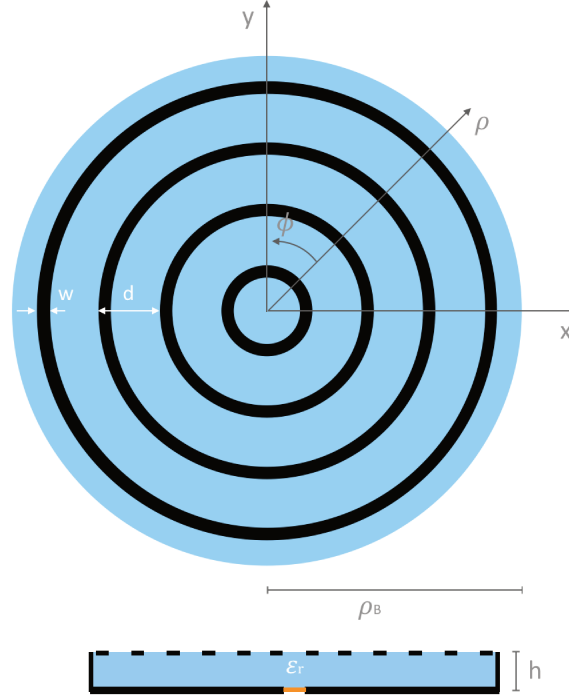


Figure 12 – Top and cross-sectional view of the considered structure along with its physical and geometrical parameters.

width w , periodicity d , substrate thickness h , substrate permittivity ϵ_r , and antenna radius ρ_B .

If we consider the 2D periodic structure presented in Figure 12 as having a value of ρ_B sufficiently big ($\lambda_0 \ll \rho_B$) we can assume $k_\rho = k_x$ since propagation is normal to metallic strips. Similarly, we assume that $k_\phi = k_y$ since propagation is along the metallic strips. Such relations become clearer by looking at Figure 13 and comparing it to Figure 12.

In summary, we want to build the equivalence of the radial 2D topology to a linear 1D-MSG presented on Figure 13. The reason that we look forward for this approximation is because the analysis of a periodic linearized structure can be restricted to a unit cell ($x = \pm d/2$). (BACCARELLI *et al.*, 2005)

Besides, when dealing with such structures, it can be seen that the wave propagates along a 1-D periodic MSG and, therefore, can be represented by Floquet waves (harmonics) (BURGHIGNOLI *et al.*, 2019). In this case, each space harmonic has a complex wavenumber

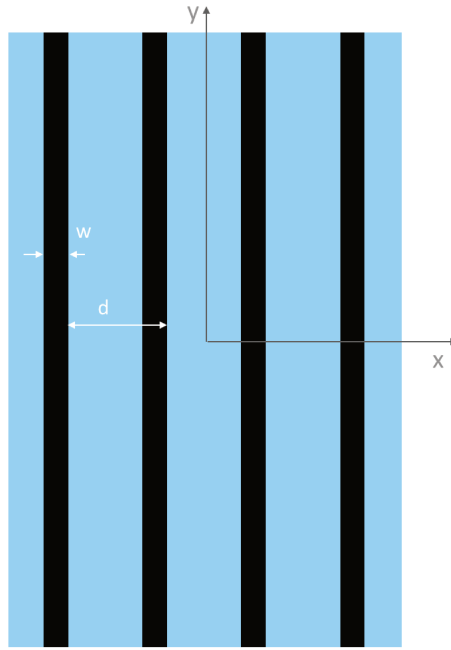


Figure 13 – 1D periodic metallic strip grating.

k_{xm} given by Equation 4.21 below.

$$k_{xm} = \beta_m + i\alpha \quad (4.21)$$

where; m is the harmonic order, and k_{xm} is analogous to $k_{\rho m}$ in a 2-D MSG case, as discussed.

In this context, β_m can also be described as:

$$\beta_m = \beta_0 + \frac{2\pi m}{d} \quad (4.22)$$

where β_0 is the fundamental harmonic's wavenumber.

4.3.1 Design Criteria

In summary, to implement the 2D periodical MSG in a Dielectric Grounded Slab we have to exploit Leaky Wave theory. Thus, such design is done taking into consideration the modal analysis of a 1D periodic structure presented on Figure 13. The modal analysis was performed using the *Eigenmode Solver* present on the software *CST Microwave Studio*.

Initially, we consider a commercial laminate with thickness $h = 3.14mm$ and having permittivity $\epsilon_r = 2.2$; and a frequency of 10 GHz. With these values, by using Equation 4.23 we can assess values for the periodicity d that can guarantee that only TM Leaky Waves radiates. (PODILCHAK *et al.*, 2010)

$$d > 2h\sqrt{\epsilon_r - 1} \quad (4.23)$$

According to (FUSCALDO *et al.*, 2018), we can also assess d as being

$$h < \frac{d}{2} \quad (4.24)$$

to ensure the first TM mode to propagate, since we have $\epsilon_r > 4/3$. (BALANIS, 2011)

These equations has allowed us to fix the periodicity d to $16mm$.

Lastly, to design the width w of the periodic MSG we have performed a parametric sweep analysis. It was found out in this analysis that a bigger value of w produces a stronger perturbation that leads to higher values for the attenuation constant α , see Figure 14. We have decided to set $w = 5mm$; which gives us $\alpha/k_0 = 0.03$.

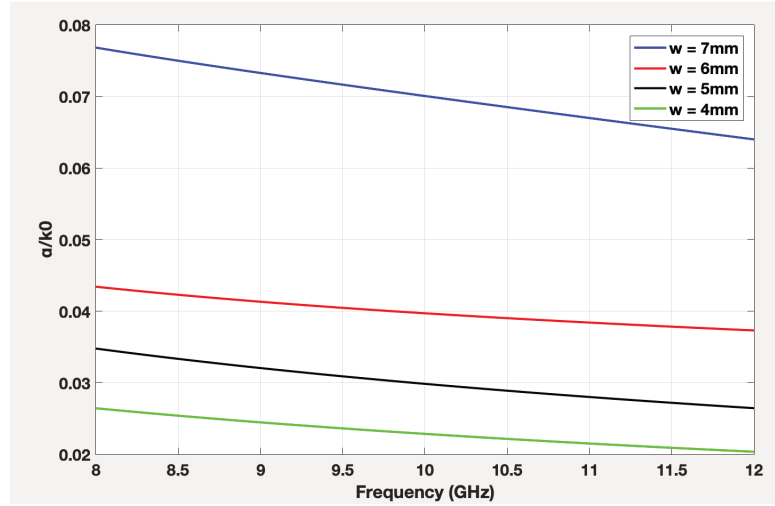


Figure 14 – Normalized attenuation constants obtained via dispersion analysis for different strip widths.

The normalized dispersion curves for β and α is presented on Figure 15. For our frequency, $10GHz$ we shall find $\beta/k_0 = 0.764$.

Since we have defined a value for the longitudinal wavenumber $k_\rho = 0.764k_0 + i0.03k_0$, we can assess the value for the final physical parameter of the antenna; its radius ρ_B . In order to do so, we recall Equation 4.12 which gives us the threshold $\rho_B \ll 0.2083$.

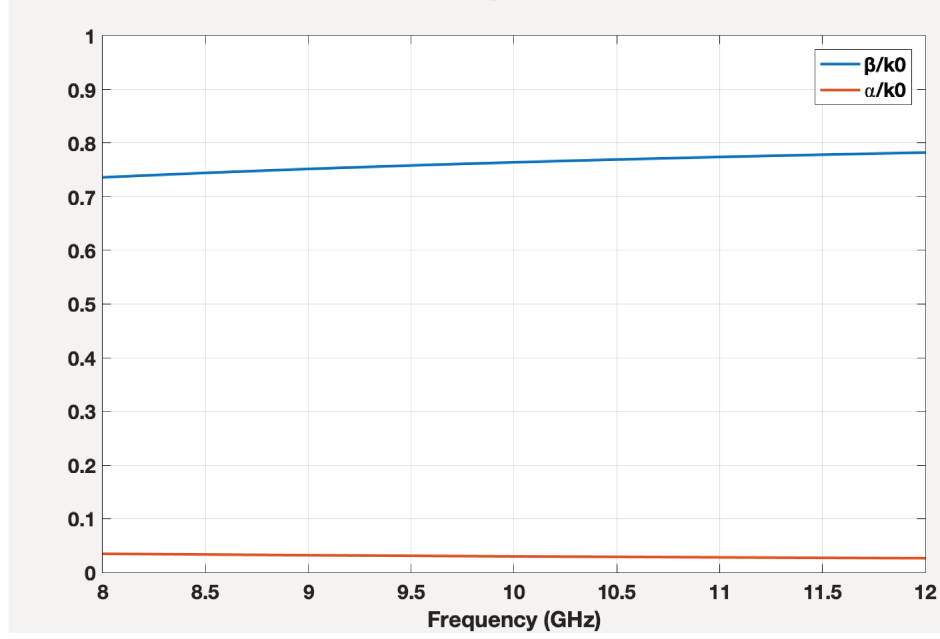


Figure 15 – Normalized phase and attenuation constants for the proposed parameters: $w = 5mm$, $d = 16mm$, $h = 3.14mm$, and $\epsilon_r = 2.2$.

Besides, we need to consider the efficiency of radiation of this antenna. This can be calculated via Equation 4.25 given by (FUSCALDO *et al.*, 2018):

$$\eta_r = 1 - e^{-4\pi\alpha\rho_B/\lambda} \quad (4.25)$$

Setting a minimal efficiency of 90%, we could find an interval for ρ_B as:

$$\rho_B > 0.1832 \quad (4.26)$$

Lastly, by using the range of values given by Equations 4.12 and 4.25; and recalling that the metallic rim must be placed at the position of one of the zeros of the Bessel Beam function, we can evaluate $J_0(k_\rho\rho)$ and define $\rho_B = 0.1838$ m; which gives us an efficiency $\eta_r = 90.07\%$.

4.3.2 Feed Design

One of the advantages of this structure is its feeding system. In contrast to the complex multi-point feeding for array configurations, a Leaky Wave Antenna constructed with a MSG over a Grounded Dielectric Slab requires solely a vertical coaxial probe with 50Ω impedance. It was constructed and modeled on CST Microwave Studio using a built-in macro to achieve

impedance matching. As presented in Figure 16, its structure is similar to the one presented by (ALBANI *et al.*, 2012).

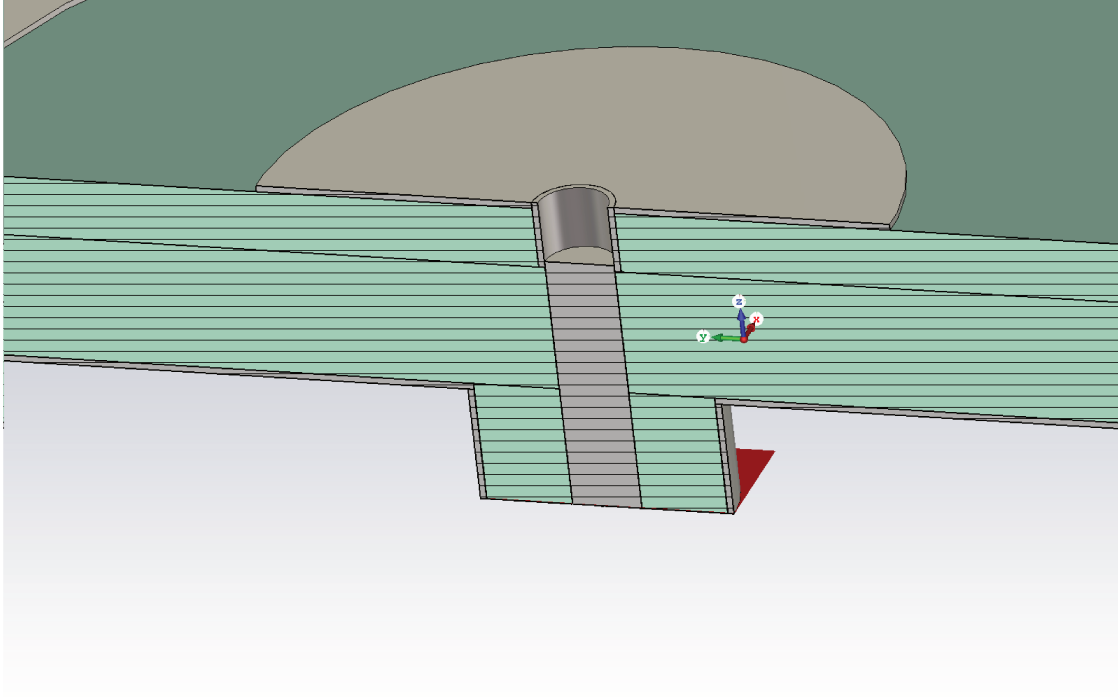


Figure 16 – Detailed view of the feeding structure simulated on CST Microwave Studio.

4.4 Simulated Results

In this section we present the results obtained via simulation on CST Microwave Studio. The simulation environment consists of open boundaries for all directions, except for the $-\hat{z}$ in which we have an electric boundary. As stated before, the antenna is fed by a coaxial cable; and, to simulate that, we have introduced a waveguide port with a default excitation to our designed 50Ω matched feed.

We are going to analyse the near field radiated by performing a full wave analysis of the antenna. To minimize the simulation time, our domain is limited to a box that contains the antenna and whose upper face is on the plane $z = 20$ cm.

At this point, we want to present the radiating field magnitude $|E_z|$. A normalized 3D view is presented on and an orthogonal projection are presented Figure 17. In both cases, we can observe a Bessel beam on the longitudinal axis z .

Observing Figure 17 b) it is possible to notice a void right on the start of the beam. Besides, by looking at Figure 17 a) we are able to see that the fields are actually starting at

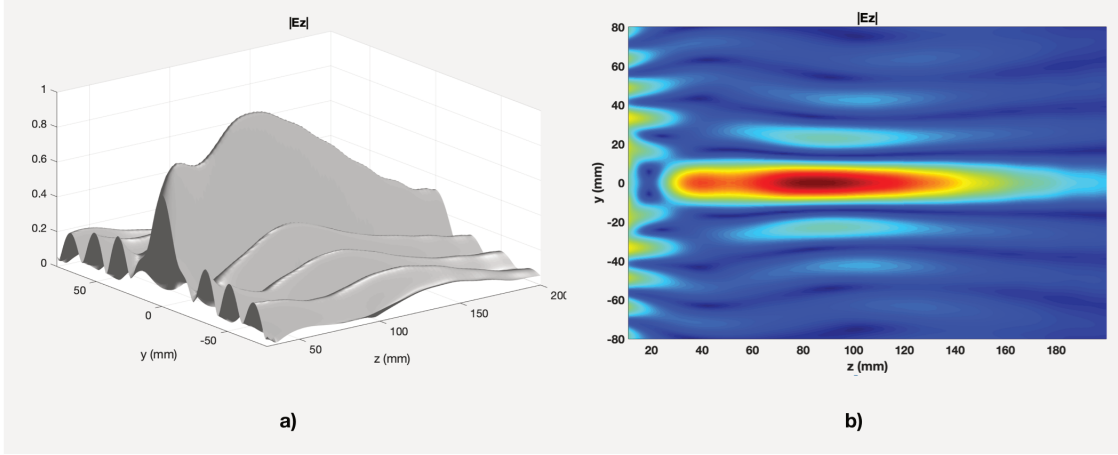


Figure 17 – For $f = 10\text{GHz}$: a) Normalized 3D visualization of the radiating field $|E_z|$. b) Color map of the absolute value of E_z .

$z = 40$ mm. It happens because while designing the antenna it was necessary to include a metallic circular region around the feeding point (see Figure 16 for more details) to prevent large forward waves losses (which do not generate the Bessel beam).

However, that works in both ways; i.e., this circular metallic region also prevents the fields from inward propagation to leak and interact to generate the beam very close to the region of the antenna.

Besides, we can investigate the propagation of this field. Firstly, we assess the value of the spot as being $\Delta\rho = 15$ mm, by looking at Figure 17 b). Then, using Equation 2.21, we can evaluate the cone angle of the beam as $\theta = 0.8694$ rad.

Lastly, we use Equation 2.22 to find the non-diffracting range for a beam with these characteristics; in this case, we found $Z = 155.3\text{mm}$. And, what we can conclude from Figure 17 b) is that the beam radiated by the simulated antenna has the theoretical propagation depth.

Besides, we would like to present $|E_z|$ on the transverse plane. In Figure 18 a 3D normalized view is provided; and, in Figure 19 a color plot is presented.

A better insight about the beam's profile was given by Figures 18 and 19. However, we can perform further examinations on this beam. For instance, we can examine Figure 19 at the line $y = 0\text{mm}$ and $z = 100\text{mm}$ to obtain its 1D profile. The result is presented on Figure 20 along with a comparison of an ideal Bessel Beam profile at the same line and with the same propagation constant k_ρ .

It can be observed on Figure 20 a good agreement between the $|E_z|$ radiated field from CST and the ideal Bessel beam. The position of the foremost maximums and zeros are

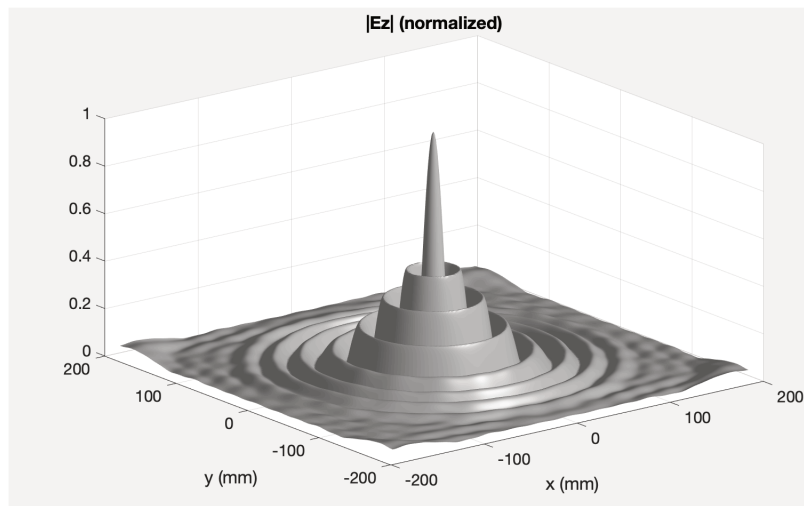


Figure 18 – Simulated 3D visualization of $|E_z|$ at the transverse plane $z = 100\text{mm}$.

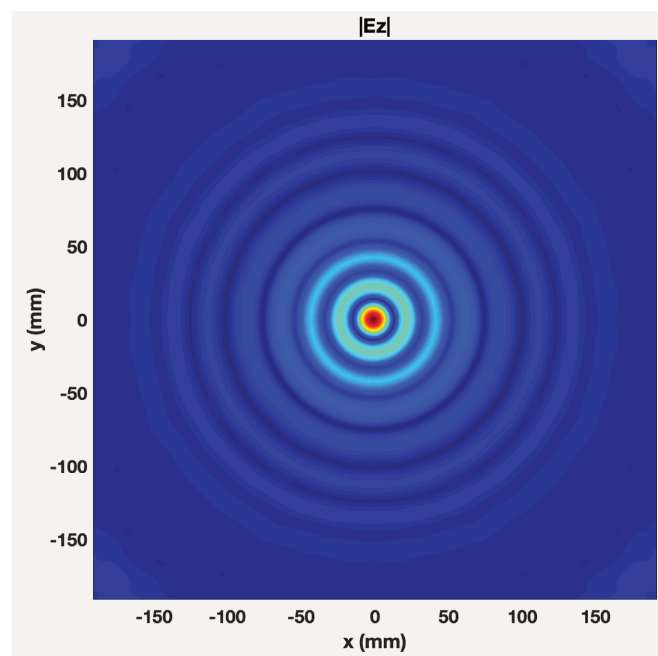


Figure 19 – Simulated 2D profile of $|E_z|$ at the transverse plane $z = 100\text{mm}$.

similar for both plots.

Hence, the results presented on Figures 17 to 20 suggest that the field radiated by the antenna, simulated on CST, agrees very well with the Bessel function and the general theory of Bessel beams. However, since we are dealing with a finite aperture, it should be noticed that for increasing values of x the beam profiles differ a lot. This feature is a direct consequence of the inward fields exited on the aperture. It was found in (ALBANI *et al.*, 2014) that the inward waves approximate the field to a Bessel Beam close to the vertical

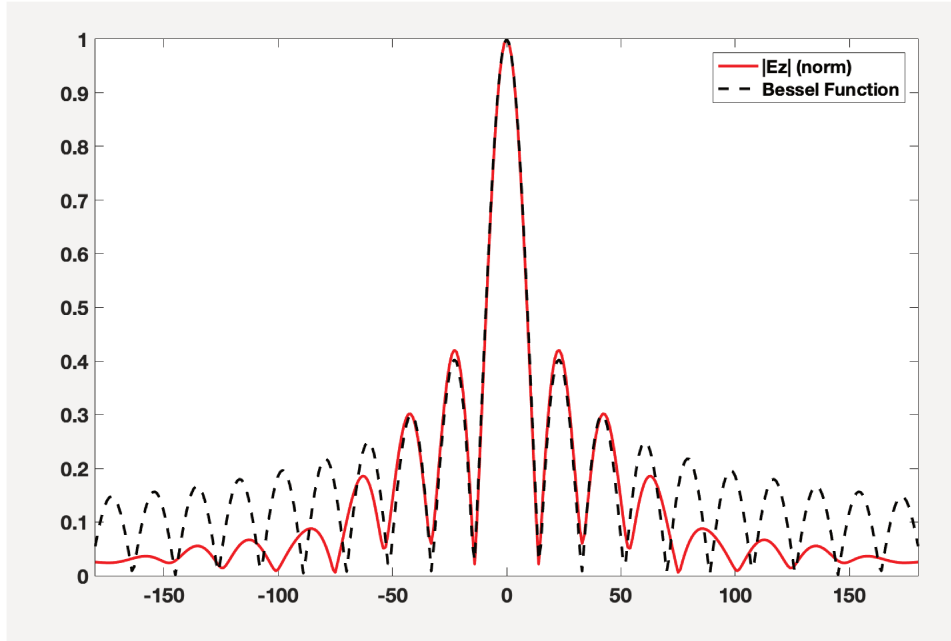


Figure 20 – 1D beam profile at the line $y = 0\text{mm}$ and $z = 100\text{mm}$ of an ideal Bessel beam (dotted black line) and the radiated beam (red line).

axis, whilst this agreement is gradually lost when moving away from the axis due to spurious radiation (as mentioned before).

We can move on to investigate the results for the transverse field. We should recall that, minding the previous section, our expected outcome is a first order Bessel beam as the pattern for $|E_\rho|$. In order to analyse this component of the electric field, we present the 2D orthogonal projection and the 2D profile on the transverse plane $z = 100\text{mm}$ on Figure 21 below.

It is clear from Figure 21 that the radiating field agrees with the theory. And, as we did before, we can obtain the 1D profile at the line $y = 0\text{mm}$ and $z = 100\text{mm}$ and compare it with an ideal first order Bessel beam (see Figure 22).

For closure, we are going to observe the resulting radiating electric field $|E|$. The orthogonal projection is presented on Figure 23.

As it can be seen in Figure 23, the resulting field still has a zeroth order Bessel beam shaping even though it is a combination of a zeroth and a first order beam. This is a direct consequence of the non-paraxiality of the field. As we were able to observe since the beginning of the section, the Bessel beam at $|E_z|$ had a spot that is ever shorter than the wavelength ($\lambda = 30\text{mm}$). Therefore, the intensity of the transverse field is much smaller than the intensity of $|E_z|$. Clearly, for our goal, it is a remarkable feature because it allow us to obtain a more

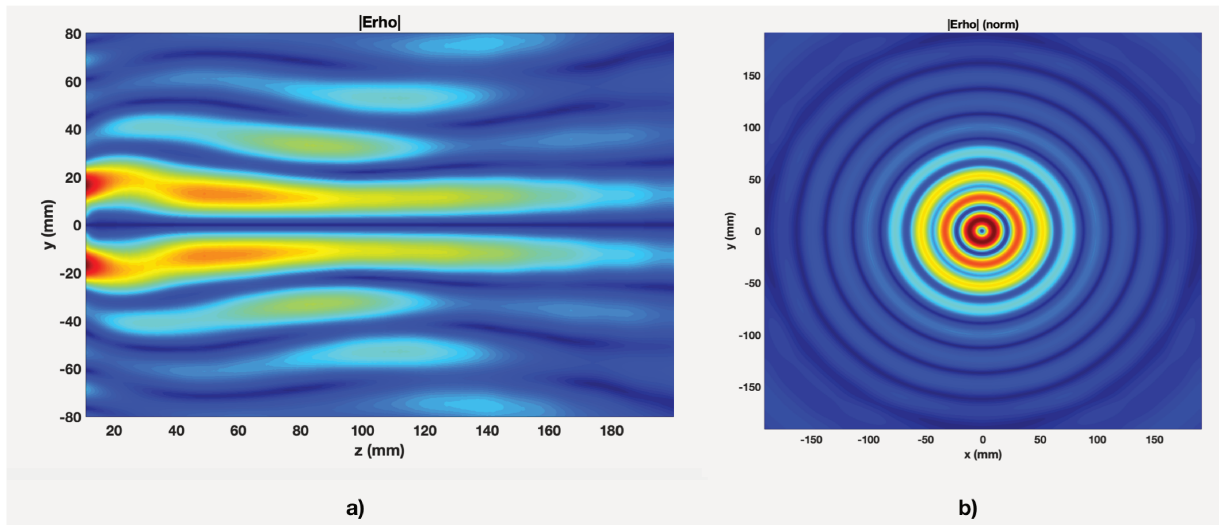


Figure 21 – a) Orthogonal projection of the transverse electric field radiated by the antenna according to simulation on *CST Microwave Studio* at the frequency of 10GHz. b) Simulated 2D profile for the transverse electric field at the transverse plane $z = 100$ mm.

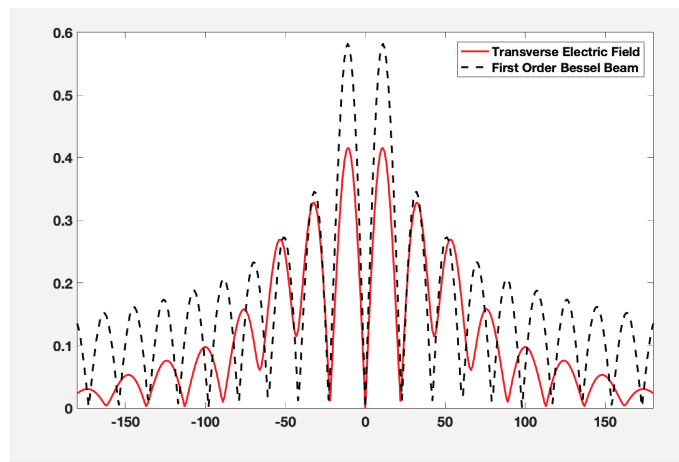


Figure 22 – 1D beam profile at the line $y = 0$ and $z = 100$ of an ideal first order Bessel beam (dotted black line) and the radiated transverse electric field (red line).

focused and zeroth order Bessel-like beam.

4.5 Further Investigations

On the previous section we have highlighted the main aspects of the simulation of the proposed antenna; and now. Here, on this section, we are going to evaluate the effects of the changes of the width w of the periodic MSG.

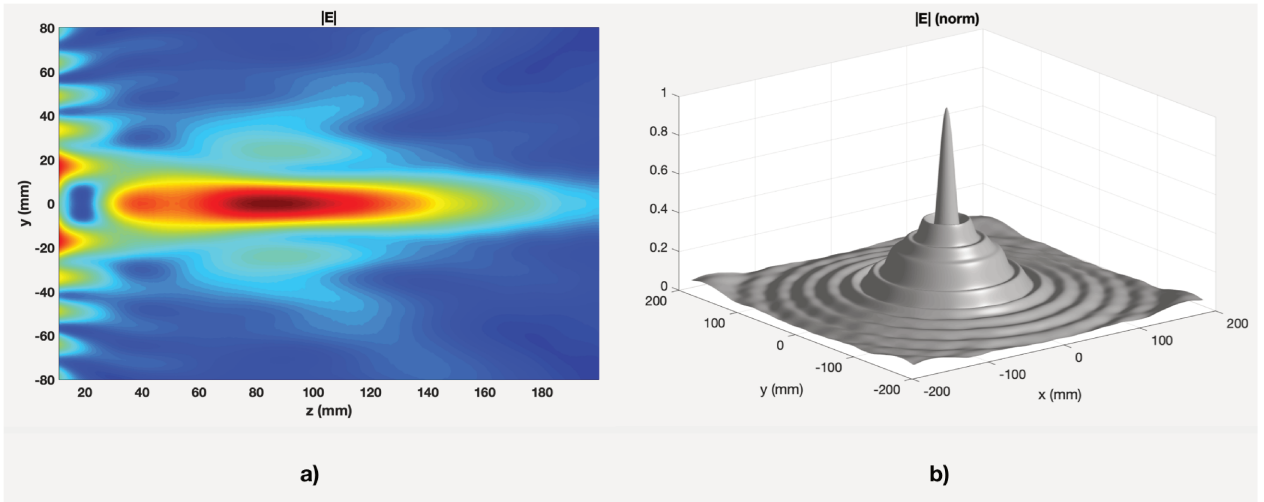


Figure 23 – a) Orthogonal projection of the absolute value of the electric field $|E|$ radiated by the antenna according to simulation on *CST Microwave Studio*. b) 3D profile of $|E|$ at the plane $z = 100$ mm.

As it has been discussed before, when changing the values of w the perturbation is changed and, therefore, the attenuation constant α is changed.

Hence, we have simulated antennas with different values for w . The results are summarized on Figure 24. The values for w and the attenuation constant α of each case are the ones presented on Figure 14.

On the first simulation - Figure 24 a) and b) - we are able to identify a similar pattern to the one presented by our antenna in Figure 17; however, it has a slightly deeper propagation depth and the main beam is visually weaker. That is a direct consequence of the smaller value for w that allows much radiation to leak away while the wave is in its outward propagation. That is reflected in the small value for α (as suggested on Figure 14) and, consequently, on the antenna efficiency below the 90% threshold.

On the second and third simulation, and also on the previous simulations, we were able to identify the impact of the the attenuation constant α . It can be observed for each of the 4 values of w that the increase of α has a detrimental effect on the propagation depth; and, for larger values of α the Bessel beam vanishes before reaching the end of the non-diffraction zone.

However, an greater value of α , and consequently a greater value of w , a smaller portion of the field is able to leak and propagate as “spurious radiation“ - radiation outside the light blue diamond shape on Figure 11. Besides, as it can be seen on Figure 24 b), d), and f), increasing values of w mitigate the typical ripples of the amplitude along the z axis

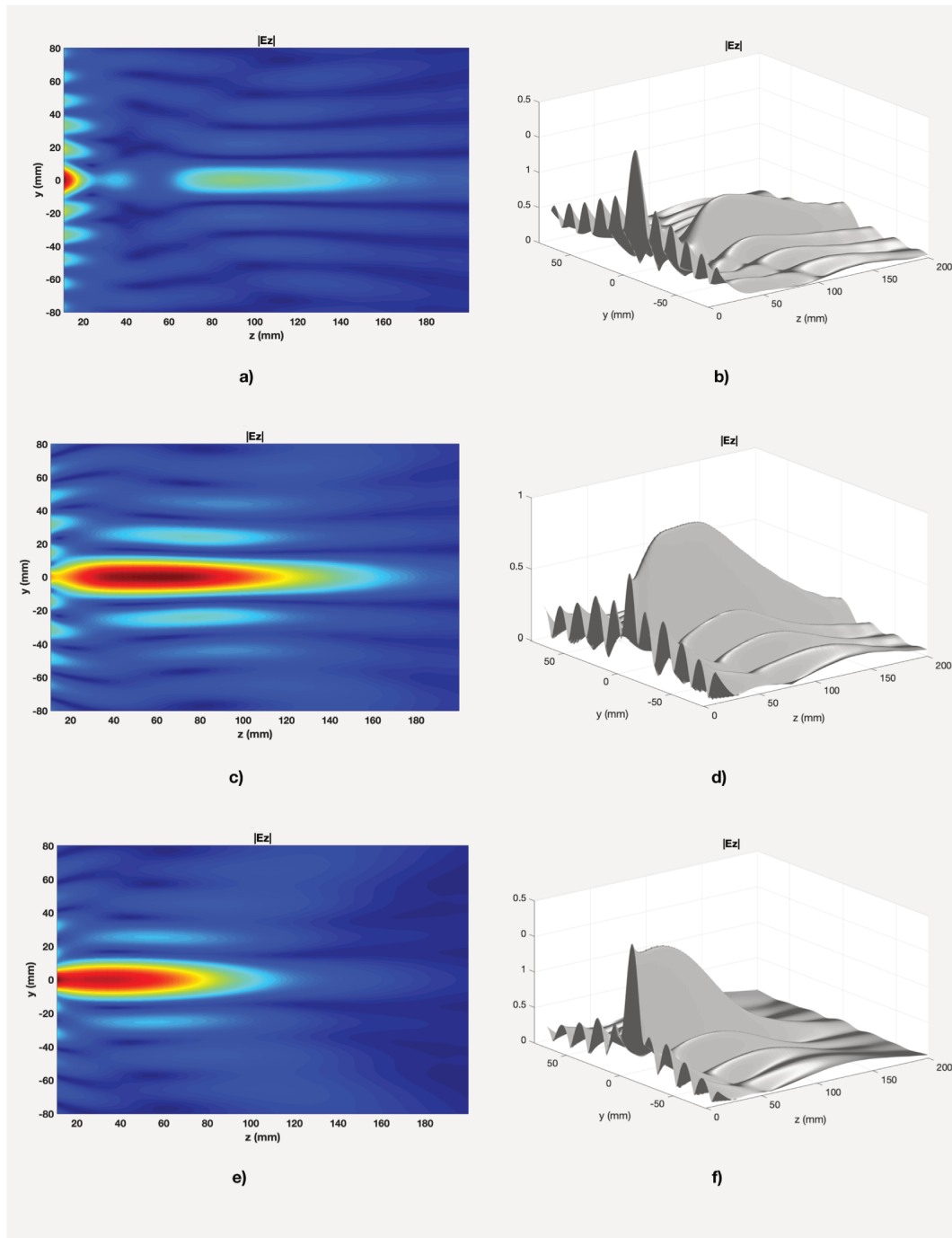


Figure 24 – a), c) and e): Orthogonal projection of $|E_z|$ radiated by the antenna according to simulation on *CST Microwave Studio* for $w = 4$ mm, $w = 6$ mm, and $w = 7$ mm, respectively. b), d) and f): Normalized 3D profile of the radiated $|E_z|$ for $w = 4$ mm, $w = 6$ mm, and $w = 7$ mm, respectively.

due to diffraction. Therefore, on these senses, a greater value of w is beneficial.

In summary, we observe a trade-off relationship between the propagation depth and

“beam quality”. And, this trade-off is controlled by the physical parameter w .

5 Millimeter and Sub-millimeter Continuous Frozen Waves in Absorbing Medium

Although the propositions and formulations to describe Continuous Frozen Waves have been set, so far they are limited in the optical frequencies and in non-absorptive propagation medium. In this section, we are aiming to obtain a scalar description to Continuous Frozen Waves when propagating through absorbing medium in millimeter and sub-millimeter frequencies.

We start by recognizing the mathematical difficulty of the problem. By looking at Equation 2.33 and analysing the situation, it is clear that once this wave is propagating in a absorbing medium (which means, $n_{ref} = n_r + in_i$) the Bessel function will now have a complex argument making its integration a demanding task.

In order to deal with that difficulty, firstly, we define $\Psi(x, y, z)$ as:

$$\Psi(\rho, z) = J_0(h\rho)e^{i\beta z} \quad (5.1)$$

Then, we write the relation for β and h :

$$n_{ref}^2 \frac{\omega^2}{c^2} = h^2 + \beta^2 \quad (5.2)$$

After that, we require h to be a real number and expressed as shown in Equation 5.3, where a is a constant. Therefore, Equation 5.3 implies that β is necessarily a complex number, since n is complex.

$$h = a \frac{\omega}{c} \quad (5.3)$$

Therefore, we must solve for β . We start by applying Equation 5.3 in Equation 5.2 which results in:

$$\beta^2 = (n_r^2 - n_i^2 - a^2) \frac{\omega^2}{c^2} + i2n_r n_i \frac{\omega^2}{c^2} \quad (5.4)$$

As a consequence of h being a real number, we have $\beta = \beta_r + i\beta_i$ and it can be expressed as shown in Equation 5.5.

$$\beta^2 = \beta_r^2 - \beta_i^2 + i2\beta_r\beta_i \quad (5.5)$$

Now, an equation system is formed using Equations 5.4 and 5.5; and, by solving it, we are going to be able to define β_r and β_i .

$$\begin{cases} \beta_r^2 - \beta_i^2 = (n_r^2 - n_i^2 - a^2) \frac{\omega^2}{c^2} \\ \beta_r\beta_i = n_r n_i \frac{\omega^2}{c^2} \end{cases} \quad (5.6)$$

Isolating β_i in line two of Equation 5.6 and substituting into line one we obtain the bi-quadratic function presented on Equation 5.7 below.

$$\beta_r^4 - \beta_r^2(n_r^2 - n_i^2 - a^2) \frac{\omega^2}{c^2} - n_r^2 n_i^2 \frac{\omega^4}{c^4} = 0 \quad (5.7)$$

Solving Equation 5.7 results in two values for β_r . The first one is real and comes from the positive $\sqrt{\Delta}$ and it is shown on Equation 5.8 below. The second one is complex and comes from the negative $\sqrt{\Delta}$; therefore, it has no physical meaning, since, by definition, β_r is the real part of β .

$$\beta_r = \sqrt{n_r^2 \frac{\omega^2}{c^2} - h^2} \quad (5.8)$$

Consequently, β_i is described as:

$$\beta_i = \frac{n_r n_i \omega^2}{c^2 \sqrt{n_r^2 \frac{\omega^2}{c^2} - h^2}} \quad (5.9)$$

Hence, we can write Equation 5.1 as:

$$\Psi(\rho, z) = J_0(h\rho) \exp \left[i \sqrt{n_r^2 \frac{\omega^2}{c^2} - h^2} z \right] \exp \left[\frac{n_r n_i \omega^2}{c^2 \sqrt{n_r^2 \frac{\omega^2}{c^2} - h^2}} z \right] \quad (5.10)$$

As a matter of fact, we can even rewrite Equation 5.1 with h in function of β_r . The result is presented in Equation 5.11 below.

$$\Psi(\rho, z) = J_0 \left(\rho \sqrt{n_r^2 \frac{\omega^2}{c^2} - \beta_r^2} \right) \exp \left[i\beta_r z \right] \exp \left[\frac{n_r n_i \omega^2}{c^2 \beta_r} z \right] \quad (5.11)$$

We need to get a continuous superposition; therefore, we calculate the integral as presented in Equation 5.12 below.

$$\Psi(\rho, z) = \int_{-n_r\omega/c}^{n_r\omega/c} S(\beta_r) J_0\left(\rho\sqrt{n_r^2\frac{\omega^2}{c^2} - \beta_r^2}\right) \exp\left[i\beta_r z\right] \exp\left[\frac{n_r n_i \omega^2}{c^2 \beta_r} z\right] d\beta_r \quad (5.12)$$

The limits of integration on Equation 5.12 are set in order to guarantee a real value for h .

At this point, we assume that the spectrum under consideration is highly non-paraxial and concentrated around β_r . So, we are able to take out the term responsible for the exponential decay (attenuation) from the integral.

The resulting equation is very similar to Equation 2.33. Therefore, the solution to the remaining integral is in the form of Equation 2.42, as presented in Equation 5.13 below.

$$\Psi(\rho, z) = \exp\left[\frac{n_r n_i \omega^2}{c^2 \beta_r} z\right] \sum_{n=-\infty}^{\infty} F\left(\frac{-2\pi n}{K}\right) \text{sinc}\left[\sqrt{\frac{n_r^2 \omega^2}{c^2} \rho^2 + \left(\frac{n_r \omega}{c} z + \pi n\right)^2}\right] \quad (5.13)$$

Analysing Equation 5.13 it is clear that the solution for beam propagating through absorbing medium is, approximately, equal to the pattern of a continuous Frozen Wave multiplied by a decaying exponential, as theory suggests.

Besides, exposing the behavior of Continuous Frozen Waves in absorbing medium, Equation 5.13 implies a way of mitigating the attenuation process; it can be achieved by simply including a growing exponential, equivalent to the decaying one, to the function $F\left(\frac{-2\pi n}{k}\right)$.

5.1 Results

In this section we shall present some examples applying our methodology. Then, we shall compare these examples to cases in which we do not apply our compensation method.

As an example, we demonstrate the case in which we simulate a propagating beam at 50 GHz, with a spot radius $\Delta\rho = 2.9\text{mm}$, with longitudinal intensity profile given by a super-Gaussian of depth 40cm, resulting on the following function $F(z)$:

$$F(z) = e^{-\left(\frac{z}{Z}\right)^8} e^{iQz} \quad (5.14)$$

For this case, $Z = 20\text{cm}$, $Q = 0.92n_r\omega_0/c$, and the index of refraction is $n = 2 + i0.02$. Figure 25 depicts the spectrum $S(k_z)$. Note that the majority of the spectrum is contained at the positive values of k_z/k .

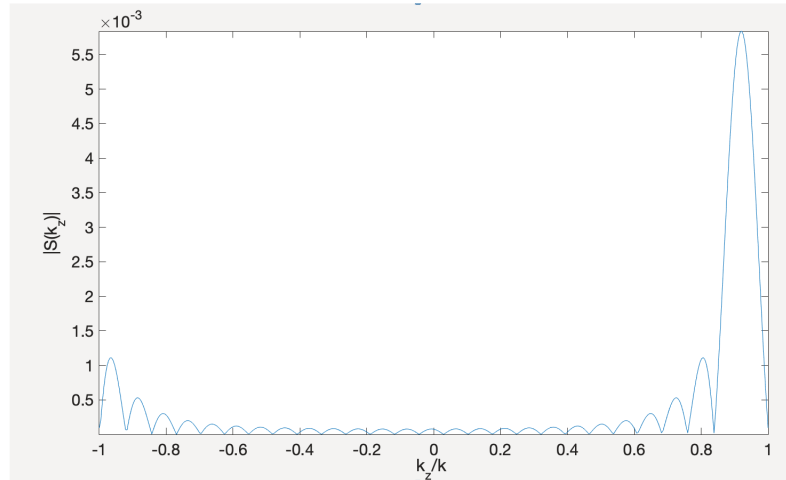


Figure 25 – Calculated spectra $S(k_z)$ for a continuous Frozen Wave at the frequency of 50GHz.

Next, we present the orthogonal projection of the beam and a 3D visualization on Figure 26.

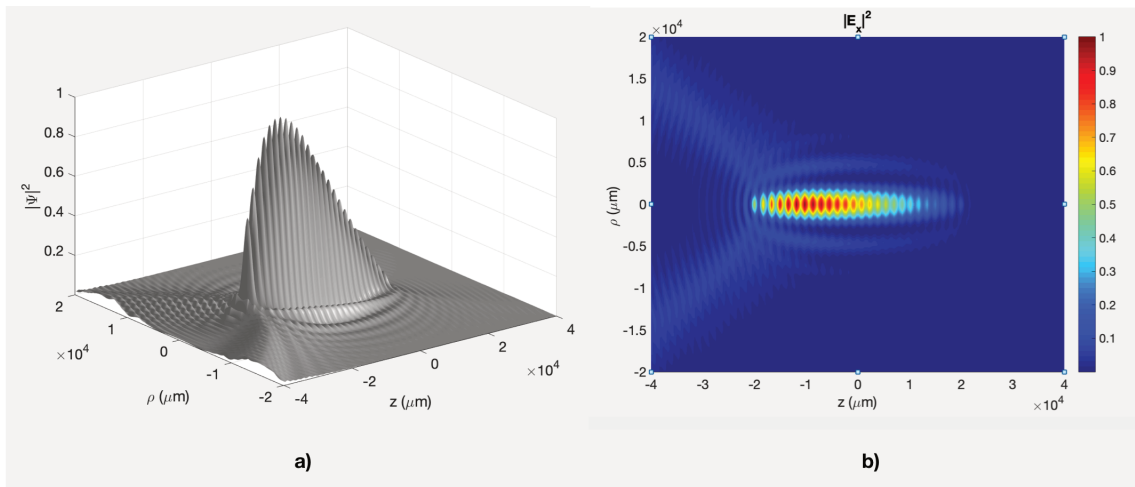


Figure 26 – a) 3D view and b) Orthogonal projection of the continuous Frozen Wave profile propagating on an absorptive medium at the frequency of 50GHz.

When looking at Figure 26 it is clear that the medium is attenuating the beam (as a consequence of its complex index of refraction). In order to mitigate these effects the interaction of the Bessel Beams that are overlapping have considerable values before the

formation of the main pattern. That is, it is necessary to input more power in order to obtain the desirable pattern. Even so, it was not achieved.

Therefore, we will apply the compensation method proposed on the last section. That said, the function $F(z)$ becomes:

$$F(z) = e^{-\left(\frac{z}{Z}\right)^8} e^{iQz} e^{z\beta_i} \quad (5.15)$$

where $\beta_i = n_i n_r \omega_0^2 c^2 / Q$ and it accounts for the attenuation.

The spectra $S(k_z)$, for this case, is presented on Figure 27.

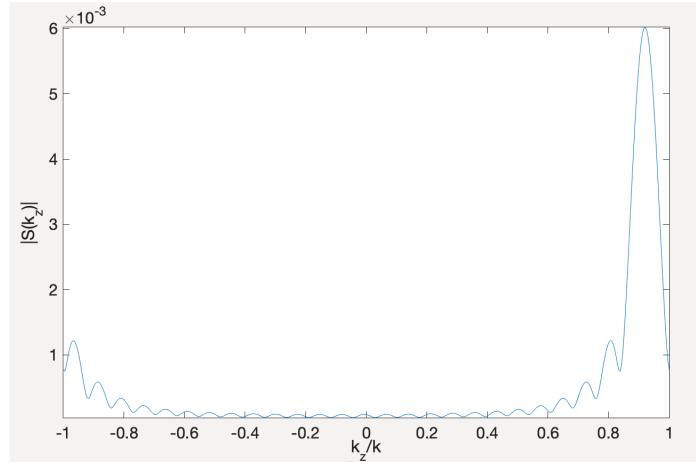


Figure 27 – Calculated spectra $S(k_z)$ for a compensated continuous Frozen Wave at the frequency of 50GHz.

Again, we present the orthogonal projection of the beam and a 3D visualization on Figure 28.

Although the absorptive nature of the propagation medium, the desirable pattern was formed (with some limitations in shape) due to the compensation method suggested previously as it can be noticed on Figure 28.

A complex index of reflection with the order of 10^{-2} is very large; in other words, we are dealing with highly absorptive material. As a matter of fact, a 50GHz plane wave would have a depth of propagation of $\delta = 2.2\text{cm}$, which is only 3.66 times the wavelength λ .

For closure, we changed the frequency to $f = 100\text{GHz}$; the super-Gaussian depth to 30cm ; and, for this case, $Z = 15\text{cm}$. Afterwards, we performed a simulation of several Continuous Frozen Waves propagating through various medium with different (and increasing) complex index of refraction ($n_i = 0.005$, $n_i = 0.01$, $n_i = 0.02$). The results are presented on Figure 29.

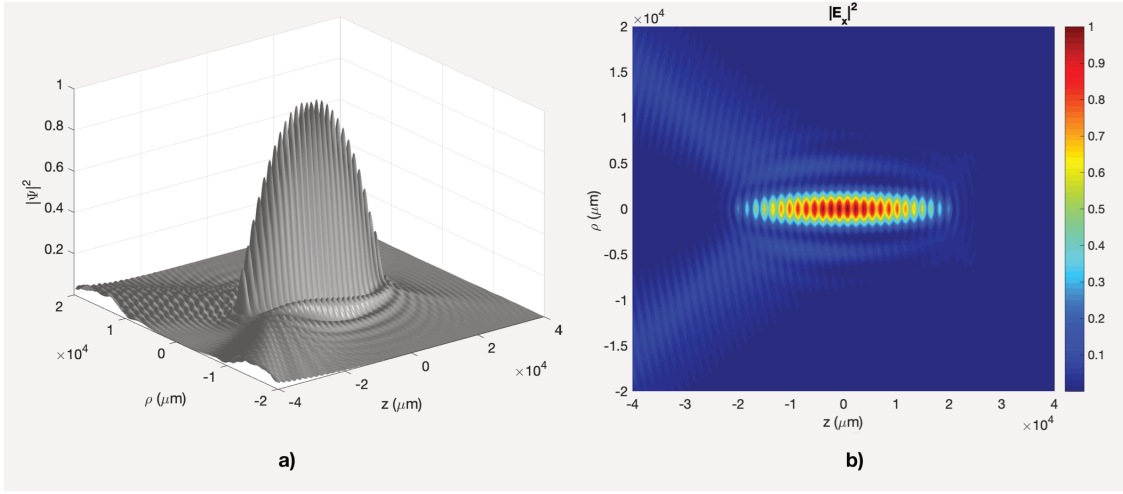


Figure 28 – a) 3D view and b) Orthogonal projection of the compensated continuous Frozen Wave profile propagating on an absorptive medium at the frequency of 50GHz.

The results highlight that our compensation technique is able to enhance beam propagation on absorptive medium.

In each case, it is clear that the non-compensated beam (Figures 29 b), d), and e)) is attenuated by the propagating medium. In fact, on the last case the beam is not able to reach the desirable propagating distance of $z = 15\text{cm}$ due to attenuation.

However, Figures 29 a), c), and e) suggest that by including a growing exponential, proportional to the attenuation, helps to obtain the desirable patterns.

In addition, on Table 2 we provide, for each case, the expected depth of propagation for a plane wave with $f = 100\text{GHz}$ and its relation to the wavelength λ .

Table 2 – Depth of propagation for a plane wave propagating through absorptive media with different complex refractive indices.

n_i	δ [cm]	δ/λ
0.005	4.39	14.633
0.01	2.2	7.333
0.02	1.1	3.667

Lastly, as it can be observed on Figure 29, the interactions of the waves that forms the main pattern on the longitudinal axis is gaining appreciable values from one case to another as we increase the complex index of refraction. We have set $n_i = 0.02$ as our limit due to the fact that for higher values these “field perturbations“ rise to the point of being equivalent to the main pattern. Therefore, this can be considered the limit of our method. We can not promote Continuous Frozen Wave propagation on medium with higher values of complex

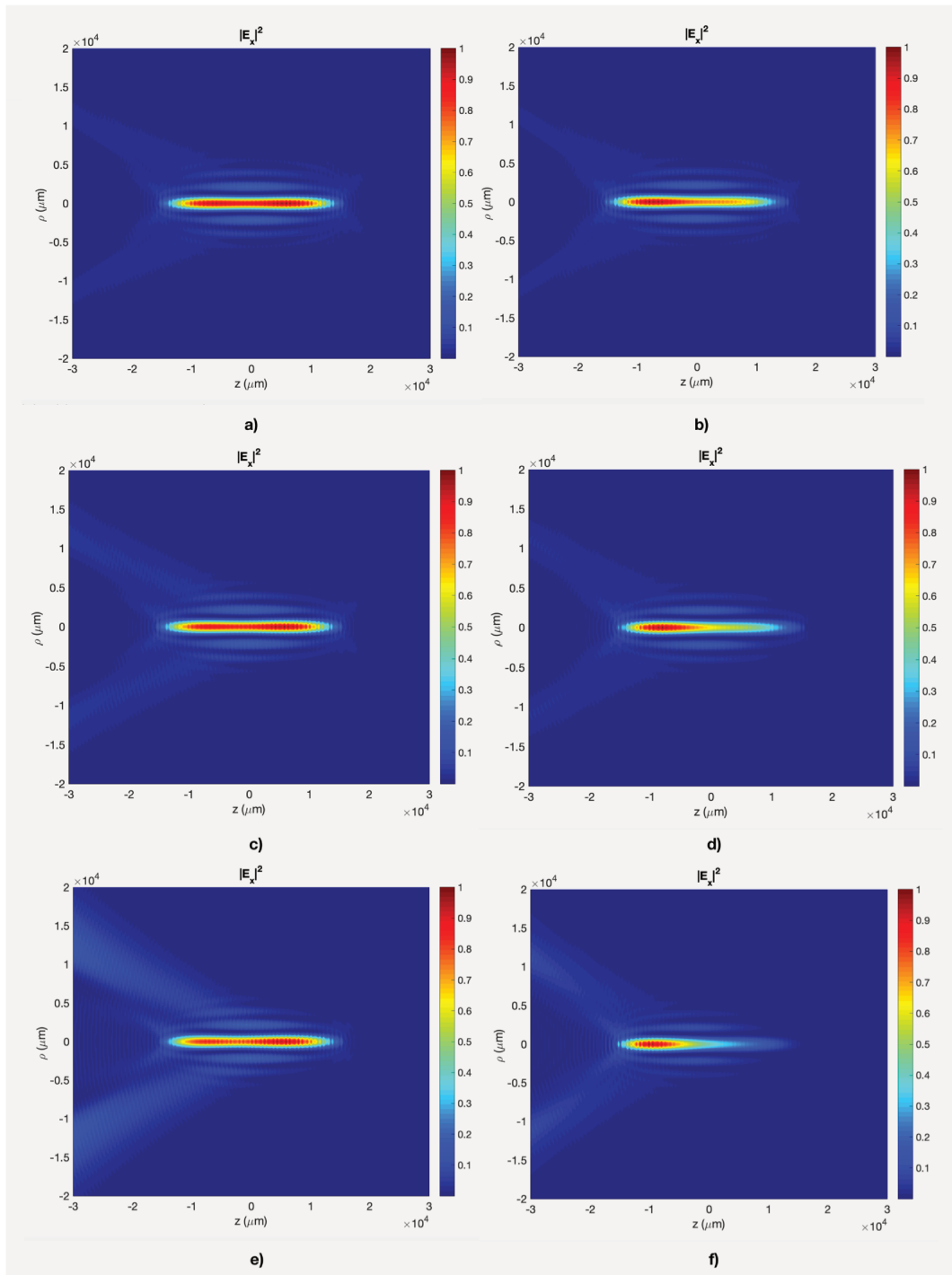


Figure 29 – a), c), and e) Orthogonal projection of the compensated continuous Frozen Wave propagating on absorptive medium with complex index $n_i = 0.005$, $n_i = 0.01$, $n_i = 0.02$, respectively. The non-compensated case is presented on b), d), and f).

index of refraction n_i .

6 Analysis of the Interactions Between Non-Diffracting Waves and Biological Tissue

The study of the dielectric properties of biological tissues in radio-frequency, microwave and terahertz has been of interest for many applications, including microwave dielectric heating, nondestructive measurement, imaging, and etc.

Information about tissue structure and how they react in contact to electromagnetic energy is important to mitigate health hazards, verify the presence of a tumor or even treat it by means of hyperthermia. (SHELLMAN *et al.*, 2008).

The purpose of this work is to obtain the current state of knowledge in terms of dielectric properties of tissues, analyse these data and present new information about the possibility of generation of non-diffractive beams - we shall focus on Bessel Beams and Frozen Waves - inside these medium.

Initially we shall retrieve the data collected by (GABRIEL *et al.*, 1996) for the electrical permittivity ϵ_r and conductivity σ for the human skin over the frequency range of 1 – 20GHz.

Next, by admitting a complex wavenumber $k = \alpha + i\kappa$ where:

$$\alpha \equiv \omega \sqrt{\frac{\epsilon\mu}{2}} \left[\sqrt{1 + \left(\frac{\sigma}{\epsilon\omega}\right)^2} + 1 \right]^{\frac{1}{2}} \quad (6.1)$$

and

$$\kappa \equiv \omega \sqrt{\frac{\epsilon\mu}{2}} \left[\sqrt{1 + \left(\frac{\sigma}{\epsilon\omega}\right)^2} - 1 \right]^{\frac{1}{2}} \quad (6.2)$$

The imaginary part of k results in a wave attenuation (decreasing amplitude for increasing values of z). And, according to (GRIFFITHS, 1962), the distance in which the amplitude is reduced by a factor of $1/e$ is called depth of propagation δ and has a value: $\delta = 1/\kappa$. The depth of propagation (blue line) for human skin is presented on Figure 30 along with the wavelength (dashed black line) for the featured range of frequency.

It is noticeable on Figure 30 that the depth of penetration is smaller than the wavelength. For this reason it is not possible to generate Frozen Waves on this medium. A Frozen

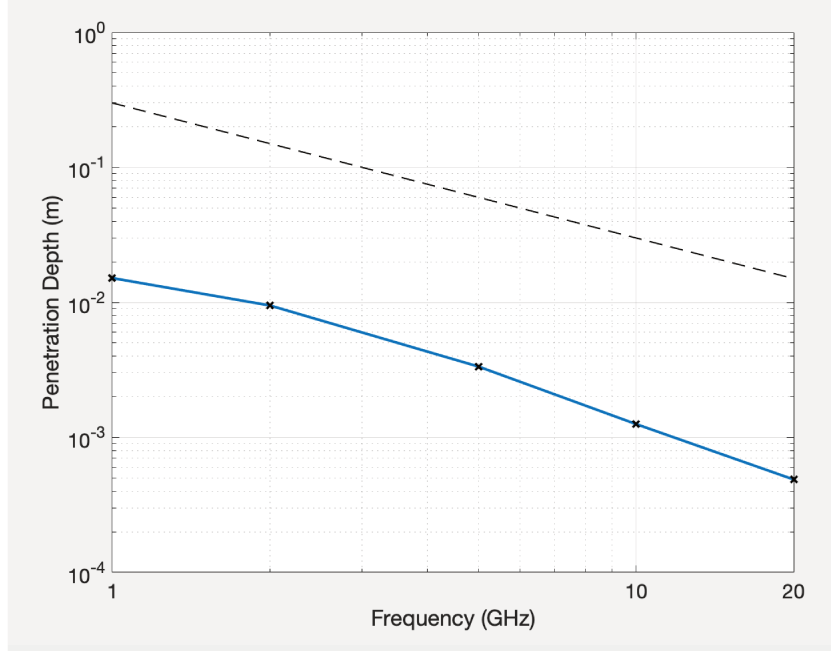


Figure 30 – Depth of penetration of a plane wave into the human skin for the range of frequency of 1GHz to 20GHz along with the wavelength λ according to the data retrieved from (GABRIEL *et al.*, 1996).

Wave is a superposition of beams that are interacting with each other while propagating; and, for this case, no beam can propagate at least for a distance λ .

We shall assess the index of reflection $n = n_r + in_i$. According to (GRIFFITHS, 1962), the real part of k determine the real part n_r as being:

$$n_r = \frac{c\alpha}{\omega} \quad (6.3)$$

Lastly, according to (HERNÁNDEZ-FIGUEROA *et al.*, 2007) we can assess n_i as:

$$n_i = \frac{c}{2\omega n_r \delta} \quad (6.4)$$

The index of reflection for the skin in the frequency range from 1 to 20GHz is presented on Figure 31.

It should be noticed that the complex part of the index of reflection n_i is higher than the ones supported by our compensating method presented on the previous section. Such values of n_i confirms our initial hypothesis of the impossibility of generation of Frozen Waves on the human skin.

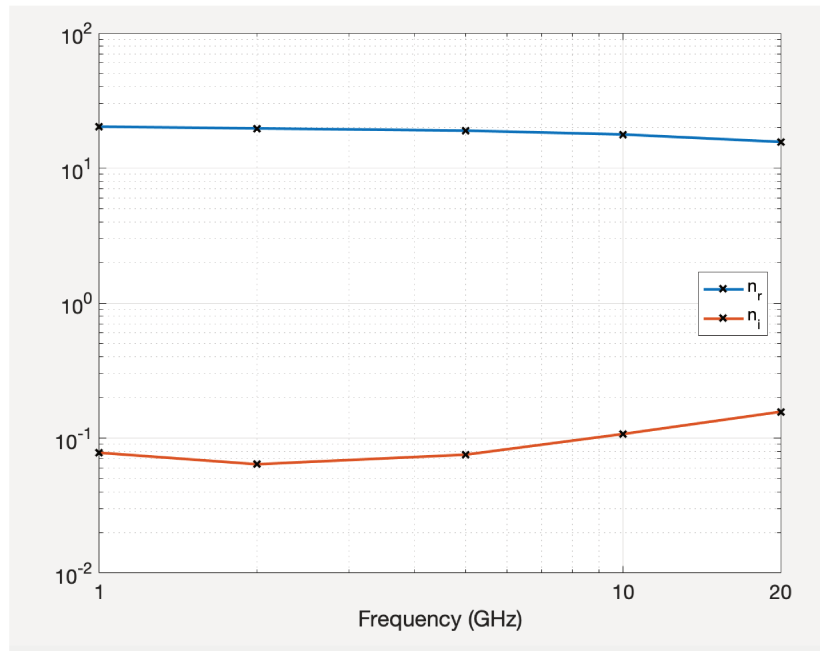


Figure 31 – Index of reflection of the human skin for the range of frequency of 1GHz to 20GHz along with the wavelength λ according to the data retrieved from (GABRIEL *et al.*, 1996).

Besides, when analysing the data collected by (GABRIEL *et al.*, 1996) it should be noticed that for all tissues studied the penetration is also very small.

Finally, we can extend this study to Terahertz frequencies. By using data for penetration and real index of reflection from (LIN, 2011) we were able to generate Figures 32 and 33.

Again, the result of the attenuation process that occurs in biological medium is too strong for the generation of Frozen Waves within it. However, as suggested by (LIN, 2011) and also in this work, when electromagnetic radiation is in contact with biological tissues heat is generated (hyperthermia). The reason for this warming is the high absorption coefficient - which leads to high attenuation coefficient - of these medium. Therefore, it is possible to use Bessel Beams to irradiate and generate heat.

Similar approaches have been developed - see (XU; WANG, 2018) and (ELKAYAL *et al.*, 2015), for instance - but not using Bessel Beams. We envision an advance on the hyperthermia techniques by using Bessel Beam due to its highly collimated profile.

Obviously, the ideal approach would be using Frozen Waves due to the control of the intensity on the longitudinal axis which would focus the radiation solely on the desirable radiation; but Bessel Beams offer advantages on the transverse plane that are already useful

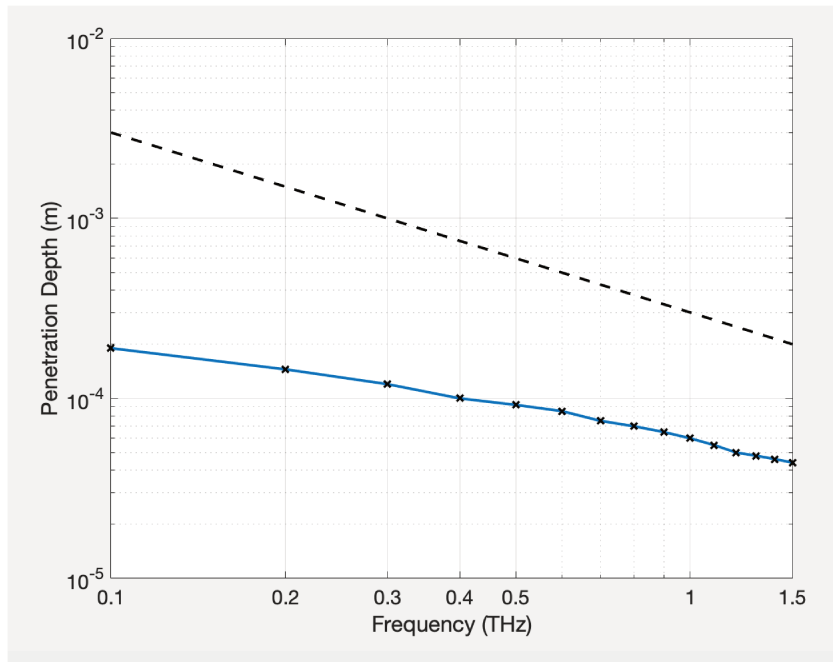


Figure 32 – Depth of penetration of a plane wave into the human skin for the range of frequency of 0.1THz to 1.5THz along with the wavelength λ according to the data retrieved from (LIN, 2011).

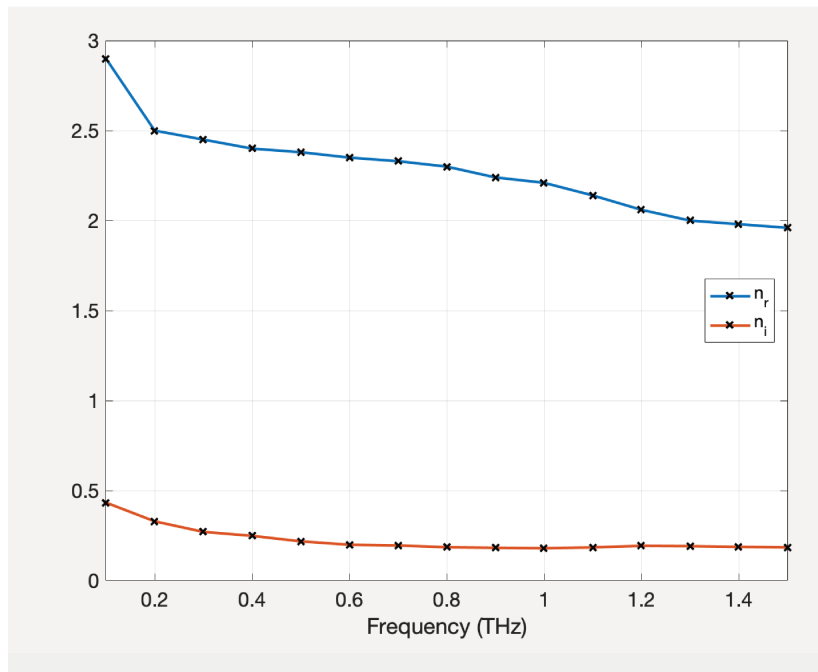


Figure 33 – Index of reflection of the human skin for the range of frequency of 0.1THz to 1.5THz along with the wavelength λ according to the data retrieved from (LIN, 2011).

in reducing the pain involved in hyperthermia treatment.

Conclusion and Future Perspectives

This masters dissertation summarizes our findings on the theoretical study of non-diffracting beams in GHz and THz, the design of an antenna capable of radiating a Bessel beam, and the interaction of Frozen Waves in millimeter and sub-millimeter wavelength with biological tissues.

On chapter 3, we were able to formulate simple, exact, and vectorial solutions to Bessel Beams emanating from a circular aperture. Our motivation for doing this was to prove that, even in millimeter and sub-millimeter wavelength, we can have a finite energy Bessel beam when truncating it by an aperture. This knowledge is essential the proceed with our path in this project, because it suggested that we could propose an antenna capable of radiating such beam.

Therefore, on chapter 4 we reviewed some of the most common Bessel beam launchers to redesign, propose, and simulate our own model. After thorough analysis, we decided to use a Leaky Wave antenna due to its simplicity in model and simulate, low-planar profile, and because it is fed by at a single point in its center.

Towards this antenna proposition, we evaluated if a Leaky Wave antenna is capable of supporting a Bessel beam; and, due to a positive outcome, we continued following this path and studied how the fields behave inside and outside (how they leak through the slits). With this knowledge we started pursuing ways for completing the design of the structure by setting its physical parameters. By completing this stage, we were able to use CST Microwave Studio to simulate the model. We could see that the radiated fields were, indeed, a Bessel beam. Lastly, we also evaluated the effects of different slits widths on our model and discovered a trade-off relationship between beam propagation depth and what we latter called “beam quality”.

On chapter 5, we studied the generation of Continuous Frozen Waves in absorbing medium envisioning its use on biological tissues to induce hyperthermic effects. Although it was later demonstrated on chapter 6 the impossibility of generate a frozen wave inside a tissue due to its low depth of propagation, we could formulate an approximate equation to describe Continuous Frozen Waves in millimeter and sub-millimeter wavelengths when they undergo mediums with high absorptive coefficients.

Finally, on chapter 6, we discovered that the attenuation process that occurs in biological medium is too strong for a Frozen Wave to be generated, but a Bessel beam could be

irradiated and generate heat. Due to its highly collimated profile, the use of a Bessel beam to induce hyperthermic effects offer advantages to the traditional methods (lower pain level and non-invasive).

6.1 Future Perspectives

This work summarizes a journey of discoveries that we have had in the past years. The knowledge obtained has the potential to lead to distinct, exciting and important paths.

On chapter 3, after showing that a Bessel beam can exist and propagate when truncated by a finite aperture, we can extend this research to assess whether a Frozen Wave exhibits the same behaviour or not. In case of a positive outcome we could also study how to generate such beam in millimeter and sub-millimeter wavelengths.

Another path would be investigating more the application of Bessel beams to generate heat in biological tissues. We could use our model on CST Microwave Studio the perform a multi-physics simulation integrating the RF and the Thermodynamics modules to attest and quantify the hyperthermical effects caused by Bessel beam irradiation.

Bibliography

- ALBANI, M.; MAZZINGHI, A.; FRENI, A. Automatic design of cp-rlsa antennas. *IEEE Transactions on Antennas and Propagation*, IEEE, v. 60, n. 12, p. 5538–5547, 2012. 58
- ALBANI, M.; PAVONE, S.; CASALETTO, M.; ETTORRE, M. Generation of non-diffractive bessel beams by inward cylindrical traveling wave aperture distributions. *Optics express*, Optical Society of America, v. 22, n. 15, p. 18354–18364, 2014. 48, 60
- ALEKSEEV, S.; RADZIEVSKY, A.; LOGANI, M.; ZISKIN, M. Millimeter wave dosimetry of human skin. *Bioelectromagnetics: Journal of the Bioelectromagnetics Society, The Society for Physical Regulation in Biology and Medicine, The European Bioelectromagnetics Association*, Wiley Online Library, v. 29, n. 1, p. 65–70, 2008. 21
- AMBROSIO, L. A.; HERNÁNDEZ-FIGUEROA, H. E. Integral localized approximation description of ordinary bessel beams and application to optical trapping forces. *Biomedical optics express*, Optical Society of America, v. 2, n. 7, p. 1893–1906, 2011. 19
- AMBROSIO, L. A.; ZAMBONI-RACHED, M. Analytical approach of ordinary frozen waves for optical trapping and micromanipulation. *Applied optics*, Optical Society of America, v. 54, n. 10, p. 2584–2593, 2015. 19
- ARLT, J.; DHOLAKIA, K. Generation of high-order bessel beams by use of an axicon. *Optics Communications*, Elsevier, v. 177, n. 1-6, p. 297–301, 2000. 47
- BACCARELLI, P.; BURGHIGNOLI, P.; FREZZA, F.; GALLI, A.; LAMPARIELLO, P.; LOVAT, G.; PAULOTTO, S. Modal properties of surface and leaky waves propagating at arbitrary angles along a metal strip grating on a grounded slab. *IEEE Transactions on Antennas and Propagation*, IEEE, v. 53, n. 1, p. 36–46, 2005. 54
- BALANIS, C. A. *Modern antenna handbook*. [S.l.]: John Wiley & Sons, 2011. 56
- BALANIS, C. A. *Advanced engineering electromagnetics*. [S.l.]: John Wiley & Sons, 2012. 26
- BORN, M.; WOLF, E. *Principles of optics: electromagnetic theory of propagation, interference and diffraction of light*. [S.l.]: Elsevier, 2013. 16
- BURGHIGNOLI, P.; COMITE, D.; FUSCALDO, W.; BACCARELLI, P.; GALLI, A. Higher-order cylindrical leaky waves—part ii: Circular array design and validations. *IEEE Transactions on Antennas and Propagation*, IEEE, v. 67, n. 11, p. 6748–6760, 2019. 54
- BUTKUS, R.; GADONAS, R.; JANUŠONIS, J.; PISKARSKAS, A.; REGELSKIS, K.; SMILGEVIČIUS, V.; STABINIS, A. Nonlinear self-reconstruction of truncated bessel beam. *Optics communications*, Elsevier, v. 206, n. 1-3, p. 201–209, 2002. 16
- CHATTRAPIBAN, N.; ROGERS, E. A.; COFIELD, D.; III, W. T. H.; ROY, R. Generation of nondiffracting bessel beams by use of a spatial light modulator. *Optics letters*, Optical Society of America, v. 28, n. 22, p. 2183–2185, 2003. 47

- COMITE, D.; FUSCALDO, W.; PODILCHAK, S. K.; RE, P. D. H.; BUENDÍA, V. G.-G.; BURGHIGNOLI, P.; BACCARELLI, P.; GALLI, A. Radially periodic leaky-wave antenna for bessel beam generation over a wide-frequency range. *IEEE Transactions on Antennas and Propagation*, IEEE, v. 66, n. 6, p. 2828–2843, 2018. 51
- DATTA, N.; ORDÓÑEZ, S. G.; GAJPL, U.; PAULIDES, M.; CREZEE, H.; GELLERMANN, J.; MARDER, D.; PURIC, E.; BODIS, S. Local hyperthermia combined with radiotherapy and/or chemotherapy: Recent advances and promises for the future. *Cancer treatment reviews*, Elsevier, v. 41, n. 9, p. 742–753, 2015. 17
- DING, D.; ZHANG, Y. Notes on the gaussian beam expansion. *The Journal of the Acoustical Society of America*, ASA, v. 116, n. 3, p. 1401–1405, 2004. 38
- DORRAH, A. H.; ZAMBONI-RACHED, M.; MOJAHEDI, M. Generating attenuation-resistant frozen waves in absorbing fluid. *Optics letters*, Optical Society of America, v. 41, n. 16, p. 3702–3705, 2016. 17, 18, 19, 22
- DORRAH, A. H.; ZAMBONI-RACHED, M.; VIEIRA, T.; GESUALDI, M.; MOJAHEDI, M. Experimental demonstration of attenuation resistant frozen waves. In: INTERNATIONAL SOCIETY FOR OPTICS AND PHOTONICS. *Laser Sources and Applications III*. [S.l.], 2016. v. 9893, p. 989311. 22
- DURNIN, J.; JR, J. M.; EBERLY, J. Diffraction-free beams. *Physical review letters*, APS, v. 58, n. 15, p. 1499, 1987. 16, 20, 47
- ELKAYAL, H. A.; ISMAIL, N. E.; LOTFY, M. Microwaves for breast cancer treatments. *Alexandria Engineering Journal*, Elsevier, v. 54, n. 4, p. 1105–1113, 2015. 75
- FUSCALDO, W. *Advanced radiating systems based on leaky waves and nondiffracting waves*. Tese (Doutorado) — Rennes 1, 2017. 47, 48
- FUSCALDO, W.; COMITE, D.; BOESSO, A.; BACCARELLI, P.; BURGHIGNOLI, P.; GALLI, A. Focusing leaky waves: a class of electromagnetic localized waves with complex spectra. *Physical Review Applied*, APS, v. 9, n. 5, p. 054005, 2018. 47, 52, 56, 57
- FUSCALDO, W.; VALERIO, G.; GALLI, A.; SAULEAU, R.; GRBIC, A.; ETTORRE, M. Higher-order leaky-mode bessel-beam launcher. *IEEE Transactions on Antennas and Propagation*, IEEE, v. 64, n. 3, p. 904–913, 2016. 17
- GABRIEL, C.; GABRIEL, S.; CORTHOUT, y. E. The dielectric properties of biological tissues: I. literature survey. *Physics in medicine & biology*, IOP Publishing, v. 41, n. 11, p. 2231, 1996. xi, xii, 73, 74, 75
- GARAY-AVENDAÑO, R. L.; ZAMBONI-RACHED, M. Exact analytic solutions of maxwell's equations describing propagating nonparaxial electromagnetic beams. *Applied optics*, Optical Society of America, v. 53, n. 20, p. 4524–4531, 2014. 31
- GARAY-AVENDAÑO, R. L.; ZAMBONI-RACHED, M. Superluminal, luminal, and subluminal nondiffracting pulses applied to free-space optical systems: theoretical description. *Applied optics*, Optical Society of America, v. 55, n. 7, p. 1786–1794, 2016. 19

- GORI, F.; GUATTARI, G.; PADOVANI, C. Bessel-gauss beams. *Optics communications*, Elsevier, v. 64, n. 6, p. 491–495, 1987. 38
- GRADSHTEYN, I. S.; RYZHIK, I. M. *Table of integrals, series, and products*. [S.l.]: Academic press, 2014. 31
- GRIFFITHS, D. J. *Introduction to electrodynamics*. [S.l.]: Prentice Hall New Jersey, 1962. 73, 74
- HERNÁNDEZ-FIGUEROA, H. E.; ZAMBONI-RACHED, M.; RECAMI, E. *Localized waves*. [S.l.]: John Wiley & Sons, 2007. v. 194. 16, 19, 21, 24, 26, 74
- ISHIMARU, A. *Electromagnetic wave propagation, radiation, and scattering: from fundamentals to applications*. [S.l.]: John Wiley & Sons, 2017. 21
- LEMAÎTRE-AUGER, P.; ABIELMONA, S.; CALOZ, C. Circular antenna array for microwave bessel beam generation. In: IEEE. *General Assembly and Scientific Symposium, 2011 XXXth URSI*. [S.l.], 2011. p. 1–4. 19, 47
- LIN, J. C. *Electromagnetic fields in biological systems*. [S.l.]: CRC press, 2011. xii, 33, 34, 35, 36, 46, 75, 76
- LÓPEZ-MARISCAL, C.; GUTIÉRREZ-VEGA, J. C. The generation of nondiffracting beams using inexpensive computer-generated holograms. *American Journal of Physics*, AAPT, v. 75, n. 1, p. 36–42, 2007. 16
- MAZZINGHI, A.; BALMA, M.; DEVONA, D.; GUARNIERI, G.; MAURIELLO, G.; ALBANI, M.; FRENI, A. Large depth of field pseudo-bessel beam generation with a rlsa antenna. *IEEE Transactions on Antennas and Propagation*, IEEE, v. 62, n. 8, p. 3911–3919, 2014. 47
- MCGLOIN, D.; DHOLAKIA, K. Bessel beams: diffraction in a new light. *Contemporary Physics*, Taylor & Francis, v. 46, n. 1, p. 15–28, 2005. 47
- MONK, S.; ARLT, J.; ROBERTSON, D.; COURTIAL, J.; PADGETT, M. The generation of bessel beams at millimetre-wave frequencies by use of an axicon. *Optics Communications*, Elsevier, v. 170, n. 4-6, p. 213–215, 1999. 47
- MUGNAI, D.; RANFAGNI, A.; RUGGERI, R. Observation of superluminal behaviors in wave propagation. *Physical review letters*, APS, v. 84, n. 21, p. 4830, 2000. 19
- NEWELL, A. *Nonlinear optics*. [S.l.]: CRC Press, 2018. 24
- PACHON, E.; ZAMBONI-RACHED, M.; DORRAH, A.; MOJAHEDI, M.; GESUALDI, M.; CABRERA, G. Architecting new diffraction-resistant light structures and their possible applications in atom guidance. *Optics express*, Optical Society of America, v. 24, n. 22, p. 25403–25408, 2016. 19
- PAL, S. K.; PEON, J.; ZEWEIL, A. H. Biological water at the protein surface: dynamical solvation probed directly with femtosecond resolution. *Proceedings of the National Academy of Sciences*, National Acad Sciences, v. 99, n. 4, p. 1763–1768, 2002. 34

- PAL, S. K.; ZEWAİL, A. H. Dynamics of water in biological recognition. *Chemical Reviews*, ACS Publications, v. 104, n. 4, p. 2099–2124, 2004. 34
- PODILCHAK, S.; ANTAR, Y.; FREUNDORFER, A.; BACCARELLI, P.; BURGHIGNOLI, P.; PAULOTTO, S.; LOVAT, G. Planar antenna for continuous beam scanning and broadside radiation by selective surface wave suppression. *Electronics letters*, IET, v. 46, n. 9, p. 613–614, 2010. 56
- PODILCHAK, S. K.; BACCARELLI, P.; BURGHIGNOLI, P.; FREUNDORFER, A. P.; ANTAR, Y. M. Analysis and design of annular microstrip-based planar periodic leaky-wave antennas. *IEEE Transactions on Antennas and Propagation*, IEEE, v. 62, n. 6, p. 2978–2991, 2014. 53
- RANFAGNI, A.; MUGNAI, D.; RUGGERI, R. Beyond the diffraction limit: Super-resolving pupils. *Journal of applied physics*, AIP, v. 95, n. 5, p. 2217–2222, 2004. 19
- RECAMI, E.; ZAMBONI-RACHED, M. Localized waves: a review. In: *Advances in Imaging and Electron Physics*. [S.l.]: Elsevier, 2009. v. 156, p. 235–353. 16
- RHOON, G. C. V.; PAULIDES, M. M.; HOLTHE, J. M. van; FRANCKENA, M. Hyperthermia by electromagnetic fields to enhanced clinical results in oncology. In: IEEE. *Engineering in Medicine and Biology Society (EMBC), 2016 IEEE 38th Annual International Conference of the*. [S.l.], 2016. p. 359–362. 21
- SALEM, M. A.; KAMEL, A. H.; NIVER, E. Microwave bessel beams generation using guided modes. *IEEE Transactions on Antennas and Propagation*, IEEE, v. 59, n. 6, p. 2241–2247, 2011. 16, 17, 19
- SHELLMAN, Y. G.; HOWE, W. R.; MILLER, L. A.; GOLDSTEIN, N. B.; PACHECO, T. R.; MAHAJAN, R. L.; LARUE, S. M.; NORRIS, D. A. Hyperthermia induces endoplasmic reticulum-mediated apoptosis in melanoma and non-melanoma skin cancer cells. *Journal of Investigative Dermatology*, Elsevier, v. 128, n. 4, p. 949–956, 2008. 46, 73
- SIEGEL, P. H. Terahertz technology in biology and medicine. *IEEE transactions on microwave theory and techniques*, IEEE, v. 52, n. 10, p. 2438–2447, 2004. 21
- SOARES, P. I.; FERREIRA, I. M.; BORGES, J. Application of hyperthermia for cancer treatment: recent patents review. In: *Topics in anti-cancer research*. [S.l.]: Bentham Science Publishers USA, 2014. v. 3, p. 342–383. 21
- STEGER, A.; BOO-CHAI, K. Interstitial laser hyperthermia: A new approach to local destruction of tumors. *Plastic and Reconstructive Surgery*, LWW, v. 86, n. 3, p. 618, 1990. 21
- STRATTON, J. Electromagnetic theory, mcgrow-hill, new-york. *Electromagnetic theory*. McGraw-Hill, New York., 1941. 16
- TAMIR, T.; OLINER, A. A. Guided complex waves. part 1: Fields at an interface. In: IET. *Proceedings of the Institution of Electrical Engineers*. [S.l.], 1963. v. 110, n. 2, p. 310–324. 50, 52

- VASARA, A.; TURUNEN, J.; FRIBERG, A. T. Realization of general nondiffracting beams with computer-generated holograms. *JOSA A*, Optical Society of America, v. 6, n. 11, p. 1748–1754, 1989. 21
- VIEIRA, T. A.; GESUALDI, M. R.; ZAMBONI-RACHED, M. Frozen waves: experimental generation. *Optics Letters*, Optical Society of America, v. 37, n. 11, p. 2034–2036, 2012. 17, 18, 19
- WELCH, A. J.; GEMERT, M. J. V. *et al.* *Optical-thermal response of laser-irradiated tissue*. [S.l.]: Springer, 2011. v. 2. 34, 35, 36, 37
- WEN, J.; BREAZEALE, M. A diffraction beam field expressed as the superposition of gaussian beams. *The Journal of the Acoustical Society of America*, ASA, v. 83, n. 5, p. 1752–1756, 1988. 38
- WILMINK, G. J.; GRUNDT, J. E. Invited review article: current state of research on biological effects of terahertz radiation. *Journal of Infrared, Millimeter, and Terahertz Waves*, Springer, v. 32, n. 10, p. 1074–1122, 2011. 33, 34
- WILMINK, G. J.; IBEY, B. L.; TONGUE, T.; SCHULKIN, B.; PERALTA, X.; RIVEST, B. D.; HAYWOOD, E. C.; ROACH, W. P. Measurement of the optical properties of skin using terahertz time-domain spectroscopic techniques. In: INTERNATIONAL SOCIETY FOR OPTICS AND PHOTONICS. *Optical Interactions with Tissues and Cells XXI*. [S.l.], 2010. v. 7562, p. 75620J. 34
- XU, L.; WANG, X. Comparison of two optimization algorithms for focused microwave breast cancer hyperthermia. In: IEEE. *2018 International Applied Computational Electromagnetics Society Symposium-China (ACES)*. [S.l.], 2018. p. 1–2. 75
- ZAMBONI-RACHED, M. Stationary optical wave fields with arbitrary longitudinal shape by superposing equal frequency bessel beams: Frozen waves. *Optics Express*, Optical Society of America, v. 12, n. 17, p. 4001–4006, 2004. 17, 18, 24, 28
- ZAMBONI-RACHED, M. Diffraction-attenuation resistant beams in absorbing media. *Optics Express*, Optical Society of America, v. 14, n. 5, p. 1804–1809, 2006. 16, 17, 18, 19, 28
- ZAMBONI-RACHED, M.; AMBROSIO, L. A.; DORRAH, A. H.; MOJAHEDI, M. Structuring light under different polarization states within micrometer domains: exact analysis from the maxwell equations. *Optics Express*, Optical Society of America, v. 25, n. 9, p. 10051–10056, 2017. 29, 31, 32
- ZAMBONI-RACHED, M.; RECAMI, E. Subluminal wave bullets: Exact localized subluminal solutions to the wave equations. *Phys. Rev. A*, American Physical Society, v. 77, p. 033824, Mar 2008. Disponível em: <<https://link.aps.org/doi/10.1103/PhysRevA.77.033824>>. 31, 32
- ZAMBONI-RACHED, M.; RECAMI, E. Parabolic antennas, and circular slot arrays, for the generation of non-diffracting beams of microwaves. *arXiv preprint arXiv:1408.5635*, 2014. 45

ZAMBONI-RACHED, M.; RECAMI, E.; BALMA, M. Simple and effective method for the analytic description of important optical beams when truncated by finite apertures. *Applied optics*, Optical Society of America, v. 51, n. 16, p. 3370–3379, 2012. 38, 40, 42

ZAMBONI-RACHED, M.; RECAMI, E.; HERNÁNDEZ-FIGUEROA, H. E. Theory of “frozen waves”: modeling the shape of stationary wave fields. *JOSA A*, Optical Society of America, v. 22, n. 11, p. 2465–2475, 2005. 17, 18, 19, 28